Simulations of the Raman-scattered O VI emission lines in symbiotic stars

H. M. Schmid[*]

Mount Stromlo and Siding Spring Observatories, Australian National University, Weston Creek, ACT 2611, Canberra, Australia

ABSTRACT

This paper investigates the Raman-scattered O VI emission lines $\lambda\lambda 6825$, 7082 in symbiotic binaries using Monte Carlo simulations. The simulations calculate the scattering path of O VI $\lambda\lambda 1032$, 1038 line photons released from an extended emission nebula. A large fraction of these photons penetrate into the extended atmosphere and the wind of the cool giant, where Raman scattering, Rayleigh scattering and absorption take place. The employed formalism includes the polarization effects and the Doppler shifts introduced by the scattering processes. As a result, the simulations provide the flux, the integrated polarization and the spectropolarimetric structure of the Raman-scattered O VI lines. Additional results are the flux properties of the O VI lines in the far UV, and maps which visualize the scattering geometry. Results are presented in detail for four model geometries. They are supplemented by many additional computations in order to explore the model parameter space.

The calculations are compared with the existing observational data of the Raman-scattered emission lines in symbiotic systems. The simulations are in general agreement with observations of the line strength, of the integrated polarization and of the phase-locked polarization variability. The simulations also reproduce the main features of the observed spectropolarimetric structure in the Raman-scattered lines. Further, the model results support the observed correlation of so-called type III profiles with systems having a red giant with strong mass-loss.

The comparison between observations and simulations also reveals the limitations of the adopted scattering model. A major shortcoming of the present models is the two-dimensional (rotationally symmetric) geometry, which was introduced to limit the computational effort. Therefore the obtained results cannot account for the three-dimensional polarization structure observed in the Raman-scattered lines of many symbiotic systems. The computations neglect gas flows and radiative transfer effects in the nebular O VI emission zone. As a result, the computations give much less spectroscopically structured Raman lines than are observed.

Nevertheless, it is found that symbiotic systems have preferentially an ionization geometry with an X-parameter $X_{H^+} \approx 1$. Roughly speaking, this 'average' shape of the ionization front does not differ strongly from a plane between the two stellar components.

Key words: polarization – radiative transfer – scattering – binaries: symbiotic – circumstellar matter.

[*]Present address: Institute of Astronomy, ETH Zentrum, CH-8092 Zürich, Switzerland.

1 INTRODUCTION

Stellar objects which exhibit simultaneously the absorption features of a cool giant and high-excitation emission lines of an ionized nebula are classified as symbiotic stars (e.g. Allen 1984). In the 1980s it has been firmly established that symbiotic stars are interacting binary systems consisting of a cool giant and a hot radiation source, which is in most cases a hot white dwarf (e.g. Kenyon 1986, Mikolajewska et al. 1988, and references therein). The orbital periods of these systems are several hundred days or longer. The hot component, which typically has a temperature $T_{hot} \approx 100\,000$ K, ionizes parts of the cool giant's wind. This produces a dense and highly ionized nebula, resulting in a strong emission-line spectrum.

Besides the emission nebula, other components of circumstellar material are observed in symbiotic systems. Enhanced IR emission due to circumstellar dust is found in D-type (D for dust) objects or symbiotic Miras (e.g. White-lock 1987). Very extended ionized regions have been mapped with radio interferometers or optical imaging techniques (e.g. Corradi & Schwarz 1993; Paresce & Hack 1994; Eyres et al. 1995). Hot, shock-heated gas is observed with X-ray telescopes (e.g. Jordan, Mürset & Werner 1994; Mürset, Jordan & Walder 1995). In symbiotic systems the circumstellar material dominates the emission in the radio, the far-IR, the visual, the UV and the X-ray wavelength ranges.

The physical and geometric properties of the circumstellar environment are largely a result of interaction phenomena, some of which seem to be extremely complex. Therefore a sound interpretation of the observational features from the circumstellar region will only be possible with physically and observationally well-based models. Good models for symbiotic systems are also a prerequisite for a reasonable determination of basic system parameters, such as the mass-loss rate of the cool component or the Zanstra-temperature of the hot component (e.g. Mürset et al. 1991).

Gradually, our understanding of the physical processes in the circumstellar environment of symbiotic systems has become clearer and the theoretical models more comprehensive. The first quantitative description of a two-dimensional ionization structure for symbiotic systems was proposed by Seaquist, Taylor & Button (1984). This analytical formalism has been further elaborated (e.g. Nussbaumer & Vogel 1987; Mürset et al. 1991). Much more detailed photoionization calculations for two-dimensional models of symbiotic systems are presented in Nussbaumer & Vogel (1990). The problem of colliding winds in symbiotic systems is treated in analytical form by Girard & Willson (1987). The complex hydrodynamical interactions in symbiotic systems are further investigated with elaborate numerical calculations in Nussbaumer & Walder (1993) and Walder (1993).

Most of these theoretical investigations suffer from a pressing lack of knowledge on the geometric structure of the innermost region in symbiotic systems. In particular, knowledge of the geometry of the ionization front, which depends in an extremely sensitive way on radiative and hydrodynamic interaction phenomena, would be very helpful.

It has been recognized recently that observational studies on the Rayleigh and Raman scattering effects in symbiotic stars may provide decisive observational constraints on interaction phenomena occurring between and close to the two stellar components (e.g. Isliker, Nussbaumer & Vogel 1989; Vogel 1991; Schmid & Schild 1990, 1994). Basic wind parameters and the shape of the interface between the ionized gas regime of the hot component and the neutral gas of the wind of the cool giant can be determined. Using spectropolarimetric data of the Raman lines, it is even expected that the geometry of the ionization front can be mapped in three dimensions (e.g. Schild & Schmid 1996). If this is indeed possible, then major progress in the understanding of interaction processes in symbiotic systems would be possible.

This is the third paper in a series where the Raman and Rayleigh scattering effects in symbiotic systems are investigated with Monte Carlo simulations.

In Schmid (1992, hereafter Paper I) the basic flux and polarization properties of the Raman-scattered emission lines are explored. Particular attention is paid to the comparison of the Raman scattering problem with previous investigations on diffusely reflected (Rayleigh-scattered) radiation from scattering atmospheres, e.g., for planetary atmospheres. Further, it is shown how the polarization vector changes due to the orbital motion of the binary system. The models in Paper I use only a very simple geometry for symbiotic systems, as they treat the cool giant as a sphere and neglect its extended structure.

The second paper (Schmid 1995, Paper II) describes Monte Carlo simulations of the Rayleigh scattering effects in the far UV for much more realistic models of symbiotic systems. Scatterings are calculated in an extended atmosphere and in that part of the wind of the cool giant which is not ionized by the hot companion. Light curves, spectra and polarization spectra are calculated for different model parameters and geometries.

In this paper we concentrate on the spectroscopic and polarimetric properties of the Raman-scattered O VI emission lines at $\lambda\lambda 6825, 7082$ Å. The calculations are based on the same Monte Carlo code as in Paper II. The present version of the code includes additionally Doppler shifts due to the systematic motion of the scattering particles. For the ionization structure we adopt the model set from Paper II.

The properties of the Raman-scattered emission lines are explored by varying different model parameters, such as the mass-loss rate of the cool giant, the widths of the initial O VI lines, or the geometry of the ionized region. The simulations provide spectropolarimetric profiles, fluxes and orbital light curves for the Raman-scattered and the direct O VI lines. These results allow an easy comparison with existing and future observations of symbiotic systems.

2 OBSERVATIONAL DATA

Up to now the emission lines at $\lambda\lambda 6825, 7082$ have been observed only in symbiotic systems. These lines are produced by a Raman scattering process of the far-UV O VI $\lambda\lambda 1032, 1038$ resonance lines by neutral hydrogen (Schmid 1989). In this process the incident O VI photon with frequency ν_i excites atomic hydrogen from its ground-state $1s^2S$

to an intermediate virtual state, from where the Raman-scattered photon v_f is emitted, leaving hydrogen in the excited state $2s^2S$. The frequency of the scattered photon is given by the principle of energy conservation $v_f = v_i - v_{if}$, where v_{if} is the frequency corresponding to the energy difference between the initial state ($1s^2S$) and final state ($2s^2S$) of hydrogen.

More than 50 per cent of the symbiotic systems show the Raman-scattered O vi lines at $\lambda\lambda6825, 7082$. They are almost always present in systems with high-excitation lines, such as [Fe vii] or [Ne v] (Allen 1979, 1980). The main prerequisite for the production of the $\lambda\lambda6825, 7082$ emission is the presence of strong O vi emission in these objects. Far-UV observations with the *Voyager* ultraviolet spectrometer (e.g. Mikolajewska et al. 1995), or more recently with the space shuttle missions *Orfeus* and *Astro-2* (Espey et al. 1995), confirmed that the O vi $\lambda\lambda1032, 1038$ emission lines are often extremely strong in symbiotic systems. Espey et al. (1995) determine for RR Tel the photon line ratios $F(\lambda132)/F(6825) \approx 12$ and $F(\lambda1038)/F(\lambda7082) \approx 36$ from simultaneous observations of the direct and Raman-scattered O vi lines.

The measured flux ratios $\Lambda = F(\lambda6825)/F(\lambda7082)$ between the two Raman lines lie in the range 2 to 10, with a mean value of $\Lambda \approx 5$ (Allen 1980). Λ tends to be larger in systems having red giants with very late spectral types, suggesting a correlation with the mass-loss rate of the cool component (Schmid & Schild 1994). For the original O vi lines a theoretical line ratio of $F(\lambda1032)/F(\lambda1038) = 2$ is expected under nebular conditions. However, in several symbiotic systems a somewhat lower line ratio of 1.2–1.8 is observed in the ns–np resonance doublets of C iv, N v and Si iv. Preliminary results from the *Orfeus* and *Astro-2* observations suggest that the same applies also to the O vi doublet. Thus Raman scattering for the $\lambda1032$ line is on average more than twice as efficient as for the $\lambda1038$ line.

The Raman-scattered O vi lines have a linewidth of about 25 Å (see Fig. 1). The large widths are a result of the Raman scattering process, which conserves the frequency displacement Δv of the incoming O vi photons. Therefore the relative widths $\Delta v/v_f$ of the Raman-scattered lines are approximately 6.7 times larger than the relative width $\Delta v/v_i$ of the initial O vi emission lines (Schmid 1989). The Raman lines often show a very complex structure with multiple components. The structure of the two components at $\lambda\lambda6825, 7082$ are, however, very similar for a given star (Fig. 1; Allen 1980). A further spectroscopic property of the Raman lines is that they are systematically redshifted by about 5 Å (Schmid 1989; Harries & Howarth 1996b).

Raman scattering is a dipole-type scattering process which produces light polarization, and strong polarization has indeed been detected in the $\lambda\lambda6825, 7082$ features (Schmid & Schild 1990). Spectropolarimetric surveys of symbiotic systems show that the Raman lines are practically always polarized, and often very strongly polarized (Schmid & Schild 1994; Harries & Howarth 1996b). Typically, the integrated line polarization is around 6 per cent. Most systems show structural variations in the polarization degree and position angle across the line profile. Maximum polarization in parts of a Raman line can exceed 15 per cent. Further, it is found that the polarization structure for a given star is always very similar in both lines. The observed
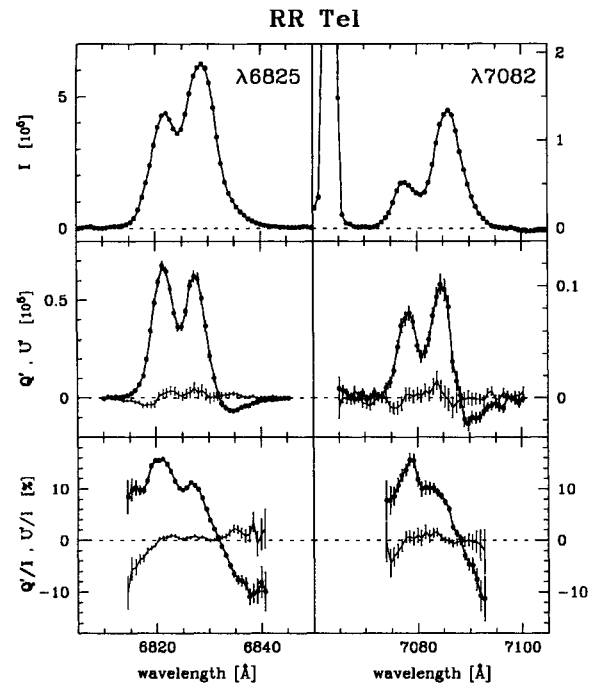
RR Tel

Figure 1. Spectropolarimetric observations of the Raman-scattered emission lines in RR Tel. The panels give the intensity I as observed photon spectrum (top), the 'rotated' Stokes parameters Q' (bold) and U' in a coordinate system aligned with the systemic position angle of polarization, and the corresponding normalized Stokes parameters Q'/I (bold) and U'/I. The data have been corrected for interstellar polarization and the stellar continuum contribution. Error bars account for the photon statistics, and the uncertainties in the interstellar correction and the continuum subtraction.

polarization profiles have some systematic properties. The blue wing tends to be more strongly polarized than the red wing. Some profiles (type III) show two distinct polarization components, having different polarization angles (often separated by about 90°). Type III profiles are preferentially seen in systems with Mira variables or late-type M giants (> M5) for which heavy mass-loss can be expected.

A good example of the observed spectropolarimetric structure in the Raman lines is plotted in Fig. 1 (type III profile). These data of RR Tel were taken with the Anglo-Australian Telescope (AAT) during the night of 1995 March 8/9. A short description of these measurements is given in Espey et al. (1995). In Fig. 1, the coordinate system for the Stokes parameters has been aligned with the systemic 14°-polarization position angle in the Raman lines of RR Tel. The same type of presentation as in Fig. 1 is used in this paper for the description of the model results.

The 'rotated' Stokes parameters suggest that the scattering geometry in RR Tel, as projected on the sky, is close to a mirror symmetry. This follows from the fact that only a small U' or U'/I signal is present. Geometric compensation of the polarization signal in a configuration with a mirror symmetry would produce polarization data with a vanishing Stokes U' or U'/I component for an aligned $Q' - U'$ coordinate system. In many symbiotic stars the observed polarization structures in the Raman-scattered lines differ strongly

from a mirror symmetry. The scattering geometry in these systems is therefore known to deviate strongly from a rotational symmetry, because any such configuration would have a mirror symmetry when projected on the sky (see Schild & Schmid 1996).

The scattering geometry in symbiotic systems rotates due to the orbital motion. Phase-locked periodic changes are therefore expected in the polarization signal of the Raman-scattered lines. Such temporal changes have been revealed with repeated observations (Harries & Howarth 1996a, 1996b; Schild & Schmid 1996).

3 MODEL DESCRIPTION

With the present Monte Carlo code we can simulate the O VI Raman scattering problem for different models of symbiotic systems. Basically the histories of many photons are followed from the source until they have escaped or are destroyed by an absorption process. After a sufficiently large number have escaped, the scattered intensity and the polarization in the Raman-scattered emission lines can be established for different lines of sight.

In our models the photons are initially released as far-UV O VI line photons from an extended emission region in the ionized nebula. These O VI photons may escape without any interaction, or they may penetrate into the neutral wind or atmosphere of the cool giant and undergo different processes: Raman scattering, Rayleigh scattering and absorption. For the Raman-scattered photons only absorption is considered. After one or several scatterings the photons may escape and be observed. In each scattering process the photon undergoes a direction and polarization change, and a Doppler shift due to the systematic motion of the scatterers.

A general guideline for the Monte Carlo technique for random walk problems is given in Cashwell & Everett (1959). Papers I and II give a detailed description on many aspects of the employed Monte Carlo code: e.g., the general scheme for calculating photon trajectories, the treatment of scattering according to the Rayleigh phase matrix, the employed geometric models for symbiotic systems, the determination of the free path lengths and an assessment of statistical errors.

The following sections give a very brief outline of the employed symbiotic star models and a description of new features of the present Monte Carlo code.

3.1 Geometric structure

An illustration of the employed model geometries is given in Fig. 2. All models are rotationally symmetric with respect to the binary axis, which is defined by the line connecting the two stars. The solid line indicates the location of the ionization front in a plane containing the binary axis. The cool giant is located in the neutral region, and the hot component in the ionized region. The dots give a projection of the three-dimensional O VI photon source emissivity. These unscattered O VI photons originate from within the higher ionized He II region. The edge of the O VI region illustrates clearly the He^{+2}–He$^+$ ionization front for the models XB, XC and XD. In model XA the He^{+2}–He$^+$ front has a shape
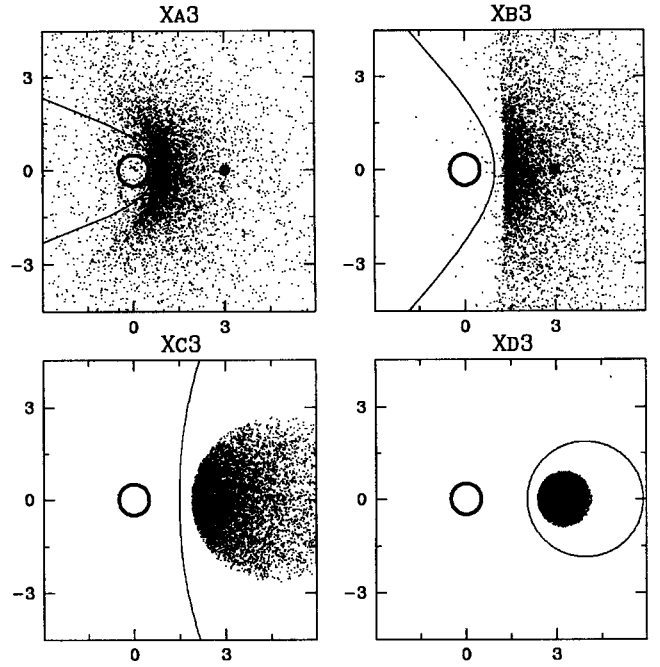
Figure 2. Geometry for the models XA ($X_{H^+}=40$), XB (4.0), XC (0.4) and XD (0.04). The hot and cool components are marked by a black point (visible only in XA3 and XB3) and a circle, respectively. The solid line gives the H$^+$–H^0 ionization front. The dots illustrate the projected source emissivity for the unscattered O VI photons (in the far UV).

like the H$^+$–H^0 front, but with a larger opening angle (see Paper II).

3.1.1 Density structure and ionization geometry

The structure of the extended atmosphere and the wind of the cool giant is described by a spherically symmetric hydrogen density distribution,

$$N_H(r) \sim \frac{(\dot{M}/v_\infty)}{r^2 - R^2},$$

where $\dot{M}$ is the mass-loss rate of the cool giant, v_∞ the terminal wind velocity, R the radius of the cool giant, and r the distance from the centre of the cool giant [Paper II, equation (1), hereafter equation (II–1)]. The corresponding velocity law for the particles in the giant's wind is (equation II–20

$$v(r) = v_\infty \left(1 - \frac{R^2}{r^2} \right).$$

Parts of this wind are ionized by the hot companion. The X-parameter description of Seaquist et al. (1984) is used for the shape of the ionization front, which is based on a simple approximation for the ionization equilibrium (see also Nussbaumer & Vogel 1987, Mürset et al. 1991 and Paper II). The dimensionless X_{H^+}-parameter is related to the ionizing photon luminosity of the hot source L_H, the binary separation p and the wind parameters of the cool giant ($\dot{M}$, v_∞) according to

$$X_{H^+} \sim p L_H \left(\frac{v_\infty}{\dot{M}}\right)^2 .$$

The X-parameter defines the geometric location $X = f(u, \theta, R_p)$ of the ionization front, as described previously (e.g. Nussbaumer & Vogel 1987; Paper II). As in Paper II, we use the modified ionization structure geometries with the additional parameter $R_p = R/p = 1/6$ to account for the finite size of the cool giant. We consider four different geometries for the H^+–H^0 ionization front A, B, C and D defined by the parameters $X_{H^+} = 40$, 4, 0.4 and 0.04 respectively.

For the O VI line-emitting region we use the same description as in Paper II for the He II and N V lines. Thus we approximate the O VI region by an X-parameter formalism for the He^{+2}–He^+ ionization equilibrium (equation II–8). For all models we use the same ratio $X_{H^+}/X_{He^{+2}} = 5.3$ between the X-parameters for the H^+ and He^{+2} ionization fronts. Such a value corresponds to a blackbody temperature $T_{hot} = 120\,000$ K for the ionizing component. Further, we assume a strong radial dependence of the line emissivity $\varepsilon(O\ VI) \sim 1/r^4$, where r measures the distance to the centre of the cool giant. This presupposes that the wind density law for the cool giant can be extrapolated into the ionized region.

We assume in all our models that the emitted O VI line radiation is isotropic and unpolarized, and has a Gaussian structure centred on the rest wavelengths 1031.93 and 1037.62 Å. This simplification neglects gas flows and radiative transfer effects in the nebular O VI zone. For the standbard models a line velocity width of $\Delta v_D = 100$ km s^{-1} (FWHM) is chosen, which is typical for the measured widths of high-excitation lines in symbiotic systems.

3.1.2 Scaling law

The scattering problem can be scaled in a simple way, as described in Paper II. The relative geometry of the photon scattering paths is not changed if the geometric dimensions of the whole model are scaled by a factor x and the particle density distribution by a factor $1/x$. The scaled density distribution is obtained through a simple scaling of the ratio between mass-loss rate and terminal wind velocity (equation II–17):

$$\frac{N_H(xr)}{x} \sim \frac{x\,(\dot{M}/v_\infty)}{(xr)^2 - (xR)^2} .$$

Thus exactly the same normalized light curves (as a function of the orbital phase), the same normalized spectra and the same polarization spectra are obtained for a model with parameters p, R, $\dot{M}$ and a model with scaled parameters xp, xR and $x\dot{M}$. Of course, the X-parameters for the ionization structure have to be the same in both models. This implies that also the photon luminosities L_H and L_{He^+} of the hot component must be scaled with the factor x (see equations II–4 and II–8).

The stellar, binary and ionization parameters of the basic model set are summarized in Table 1. For the scalefactor $x = 1$ the model parameters are identical to the S-models described in Paper II.

Symbiotic systems can be divided into two groups according to their infrared colours: S-types and D-types (Webster

Table 1. Model parameters for the basic model set X_A3, X_B3, X_C3 and X_D3.

MODELS X (basic model set)	
separation	$p_x = x \cdot 3 \cdot 10^{13}$ cm $= x \cdot 2$ AU
system mass	$M_{tot} = 2$ M$_\odot$
orbital period	$P_x = x^{3/2} \cdot 2$ yr
temperature of hot star	$T_{hot} = 120\,000$ K
luminosity of hot star	$L_x = x \cdot 1000$ L$_\odot = x \cdot L_3$
radius of red giant	$R_x = x \cdot 5 \cdot 10^{12}$ cm $= 1/6\,p_x$
terminal wind velocity	$v_\infty = 20$ km/s
O VI velocity width (FWHM)	$\Delta v_D = 100$ km/s
mass loss of red giant	$\dot{M}_x = x \cdot \dot{M}_3(X_{H+})$
$\quad$X$_A$3 $\quad X_{H+} = 40$	$\dot{M}_x = x \cdot 1.21 \cdot 10^{-7}$ M$_\odot$/yr
$\quad$X$_B$3 $\quad X_{H+} = 4$	$\dot{M}_x = x \cdot 3.84 \cdot 10^{-7}$ M$_\odot$/yr
$\quad$X$_C$3 $\quad X_{H+} = 0.4$	$\dot{M}_x = x \cdot 1.21 \cdot 10^{-6}$ M$_\odot$/yr
$\quad$X$_D$3 $\quad X_{H+} = 0.04$	$\dot{M}_x = x \cdot 3.84 \cdot 10^{-6}$ M$_\odot$/yr

& Allen 1975). S-type systems have IR colours typical for the photosphere of a cool stellar source, while D-type systems show strong dust emission. The S-type symbiotic systems are binaries with relatively short orbital periods $P \approx 1$–3 yr, a normal M giant (sometimes K or G giant) as cool component, and a compact emission nebula with high density $N_e \approx 10^9$ cm^{-3}. D-type systems are more extended binaries which contain a Mira variable as cool component and a lower density nebula, $N_e \approx 10^6$ cm^{-3}. The orbital periods are probably very long $P \gg 10$ yr.

Typical parameters for S-type symbiotic systems are obtained for models with a scaling factor x in the range 0.6–1.3. This gives systems with orbital periods between 1 and 3 yr and red giant radii between 40 and 90 R$_\odot$. These radii correspond to giants with spectral types between M0III and M5III (Schmidt-Kaler 1982). D-type systems contain often a Mira variable as cool component, and the known pulsation periods lie in the range 300–600 d (Whitelock 1987). Angular diameter measurements indicate photospheric radii in the range 400–500 R$_\odot$ for nearby Mira variables (Haniff, Scholz & Tuthill 1995). Thus scaling factors in the range $x = 4$–10 may be appropriate for D-type symbiotic systems. Such x-values imply orbital periods between 16 and 63 yr, and stellar radii of 300 to 700 R$_\odot$.

3.1.3 Model system – observer's system

The simulations provide values of the intensity $I(\alpha)$ and the Stokes parameter $Q(\alpha)$ as a function of the phase angle α ($0° \leq \alpha \leq 180°$). The phase angle α is defined as angle between the line of sight and the binary axis connecting the two stars. The functions $I(\alpha)$ and $Q(\alpha)$ represent half an eclipse light curve, where the hot component is in front of the cool component for $\alpha = 0°$ and behind it for $\alpha = 180°$.

Spectropolarimetric observations are described in celestial coordinates by the Stokes parameters I_c, Q_c and U_c, and the phase dependence is expressed as a function of the orbital angle ω.

The conversion of parameters between the model system and the observer's system is described in detail in Paper I (section 3.3.3) for circular binary orbits. During an orbit the phase angle will wave between a minimum $\alpha_{min} = 90° - \beta$ and a maximum value $\alpha_{max} = 90° + \beta$. The corresponding conver-

sion $\omega \rightarrow \alpha$ depends on the inclination of the orbital plane i (equation 1–7). Further, the apparent direction of the binary axis ϖ_c rotates on the sky as a result of the binary motion. The direction ϖ_c is defined by the orbital angle ω, the inclination i and the orientation of the line of nodes Ω (equation 1–8). Thus observable quantities can be constructed from the model results according to (equation 1–9):

$$I_c(\omega, i) = I(\alpha_{\omega,i}),$$

$$Q_c(\omega, i, \Omega) = -Q(\alpha_{\omega,i}) \cos 2\varpi_c,$$

$$U_c(\omega, i, \Omega) = -Q(\alpha_{\omega,i}) \sin 2\varpi_c.$$

Unlike in Paper I, we use here the convention that $Q(\alpha)$ is positive for a polarization perpendicular to the binary axis.

3.2   Scattering and absorption processes

The employed symbiotic system models have two zones: the ionized region and the giant's neutral wind including its atmosphere.

Rayleigh and Raman scattering of O VI photons by atomic hydrogen is considered in the neutral part of the giant's wind. For this neutral region we include an absorption opacity for the O VI lines and the red Raman-scattered lines. In the ionized zone we neglect scatterings and absorptions.

The cross-sections per volume element for all these photon processes are assumed to be proportional to the H^0 density. This simplifies the calculations considerably, because optical depths are defined by the corresponding H^0 column density.

3.2.1   Raman and Rayleigh scattering cross-sections

The total Rayleigh and Raman scattering cross-sections for neutral hydrogen depend on wavelength. For the individual O VI lines the wavelength dependency of the cross-sections are neglected. We adopt a 'mean' value for each O VI line, as given in Schmid (1989):

$$\sigma_{Ray}(\lambda 1032) = 23, \qquad \sigma_{Ram}(\lambda 1032) = 4.4,$$

$$\sigma_{Ray}(\lambda 1038) = 4.4, \qquad \sigma_{Ram}(\lambda 1038) = 1.3, \qquad (1)$$

$$\text{units} : [10^{-24} \text{ cm}^2].$$

These cross-sections were calculated from a readily applicable expression in terms of oscillator strengths given by Isliker et al. (1989). The same cross-sections are also evaluated in Sadeghpour & Dalgarno (1992), who obtained values which lie within 25 per cent of those given in equation (1).

Rayleigh and Raman scattering are dipole-type scattering processes. In the Monte Carlo code the scatterings are treated according to the Rayleigh phase matrix, which includes the Stokes Q and U parameters for the scattering polarization (see Paper I).

3.2.2   Absorption opacities

In the present simulations a very simple treatment for the absorption opacities is made. We employ for the basic

model set the standard values $\kappa_{UV} = 1.0 \times 10^{-24} \text{ cm}^{-2} \text{ H}^{-1}$ for the far-UV O VI lines, and $\kappa_{red} = 0.1 \times 10^{-24} \text{ cm}^{-2} \text{ H}^{-1}$ for the Raman-scattered lines. Other values are used for the models presented in Section 4.6.2.

Unfortunately, the absorption opacities at the wavelengths of the O VI lines $\lambda\lambda 1032, 1038$ are not well known for atmospheres of cool giants. A further complication is that both κ_{UV} and κ_{red} may be changed in symbiotic systems due to irradiation and interaction processes caused by the hot companion. In the far UV, dust scattering and absorption in the wind of the cool giant may be very important, especially in the dusty D-type systems. O VI photon absorptions may also be frequent due to photoionization of neutral atoms, or due to atomic and molecular line transitions. For example, absorptions by C II and molecular H_2 may affect the weaker O VI line at $\lambda 1038$. A pronounced wavelength dependency of the κ_{red} opacities in M-type giants due to the TiO molecule may also exist. However, the great similarity in the spectroscopic and polarimetric structure of the two Raman-scattered lines $\lambda\lambda 6825, 7082$ (see Section 2) indicates that selective absorption in only one component is not a dominant effect.

Knowledge of the exact value of the absorption opacities in the giant's atmosphere and wind is not so important for the Raman scattering problem as long as κ_{uv} and κ_{red} are considerably smaller than the Rayleigh and Raman scattering opacities. In this case, the photon paths are predominately determined by Rayleigh and Raman scatterings, and the escape probability from the scattering region.

3.2.3   Doppler shifts

The moving scatterers in the giant's wind cause a Doppler shift in the photon frequency or wavelength. In the Monte Carlo simulations only the systematic motion of the H^0 atoms in the giant's wind $v(r)$ is taken into account. Thermal motions of the particles are expected to be much smaller than the typical wind velocity $v_\infty \approx 20 \text{ km s}^{-1}$, and possible turbulent velocities are neglected. For Rayleigh scattering the frequency of the scattered photon v_f in the observer's frame is calculated according to (neglecting second-order terms)

$$v_f = v_i \left[1 + \frac{v(r)}{c} (\cos \psi_f - \cos \psi_i) \right], \qquad (2)$$

where v_i is the frequency of the incoming photon, and c is the speed of light. ψ_f and ψ_i are the angles between the motion direction of the scatterer and the propagation directions of the scattered and incoming photons respectively.

Accordingly, the Doppler shift in the non-elastic Raman scattering process is

$$v_f = (v_i - v_{if}) \left[1 + \frac{v(r)}{c} \left(\cos \psi_f - \frac{v_i}{v_i - v_{if}} \cos \psi_i \right) \right]. \qquad (3)$$

The frequency corresponding to the energy difference between the initial state $1s^2S$ and the final state $2s^2S$ of atomic hydrogen is $v_{if} = 2.466\,06 \times 10^{15}$ Hz. The Raman frequency $v_f = v_i - v_{if}$ would result in a Raman scattering by neutral hydrogen, if no Doppler shift is introduced in the scattering process. In the case of the O VI lines, the factor
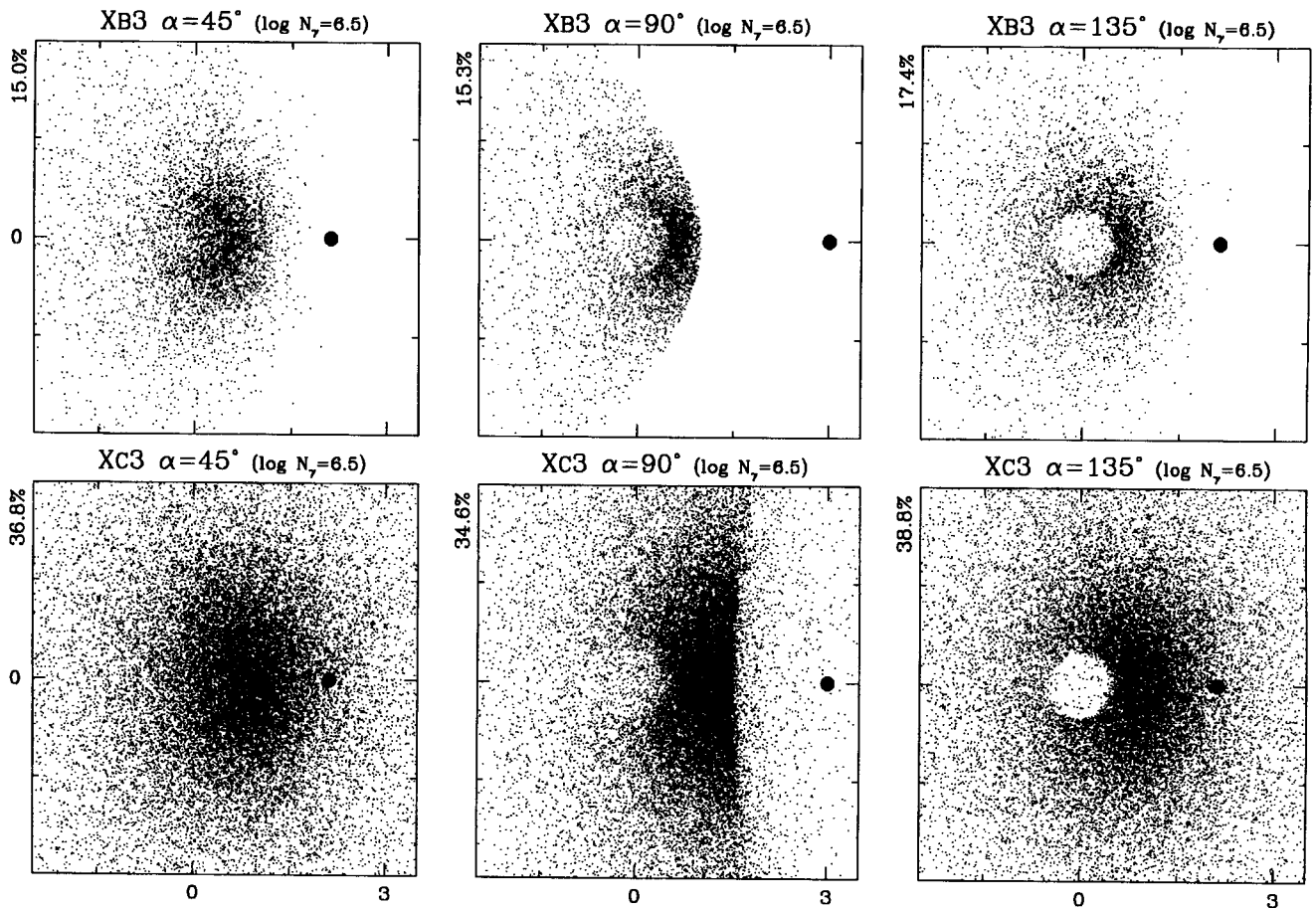
Figure 3. Maps of the Raman-scattered radiation $\lambda6825$ for the geometric models X_B3 and X_C3 at phase angles 45°, 90° (quadrature) and 135°. N_i is the photon luminosity of the O vi source in the Monte Carlo simulations. The number outside the upper-left corner of each panel indicates the fraction of Raman-scattered photons escaping from outside the plot boundaries.

$v_i/(v_i - v_{if})$ is 6.62 for the $\lambda1032 \rightarrow \lambda6825$ conversion, and 6.83 for the $\lambda1038 \rightarrow \lambda7082$ conversion. This means that the relative Doppler shifts due to the propagation direction of the incoming photon and the motion of the scattering particle $v(r)\cos\psi_i/c$ are multiplied by these factors in the Raman scattering process.

4 RESULTS

4.1 Imaging the Raman-scattered radiation

Scattering maps of the Raman scattered photons $\lambda6825$ are given in Fig. 3 for the models X_B3 and X_C3. The systems are seen for three phase angles $\alpha = 45°$, 90° and 135°. The location of the ionizing component is indicated by a filled dot. In all plots the centre of the cool component is at (0, 0). The O vi $\lambda1032$ line radiation originates in an extended zone in the ionized region, as described in Section 3 and shown in Fig. 1. A fraction of these photons penetrate into the neutral H^0 region and may undergo a Raman scattering process. Fig. 3 shows the geometric origin of the escaping Raman-scattered photons. The plots give only the central region of the systems. The fraction of photons escaping from outside the plotted area is indicated for each panel.

We discuss first the scattering maps of model X_B3, where Raman scattering occurs only in the cone-shaped neutral region around the cool giant. At phase angle $\alpha = 45°$, the extended O vi emission region is predominately in front and to the right of the cool giant. The escaping Raman photons are thus back-scattered photons from the H^0 region. The quadrature phase ($\alpha = 90°$) illustrates well the scattering geometry, with the cone-shaped neutral region from where the Raman-scattered photons originate. High Raman scattering emissivities are produced in the neutral region between the two stellar components, where high-density gas of neutral hydrogen is strongly irradiated by O vi photons. Also visible is the shadow of the cool giant, which occults parts of the scattering region. At phase $\alpha = 135°$, a substantial fraction of the scattering region lies behind the cool component. The main feature of the corresponding map is therefore the occulting stellar disc of the cool component. Apart from this obscuration, the 'outer' scattering region shows no obvious difference between the phase angles $\alpha = 135°$ and 45°.

In model X_C3 the cool component has a higher mass-loss rate (factor 3.16) than in X_B3. The neutral region has a correspondingly higher density and is more extended. Therefore many more Raman scatterings occur in model

Xc3. In this model, 13.6 per cent of the initially released O vi λ1032 photons are converted to λ6825 photons. The corresponding number for model Xв3 is only 2.1 per cent.

Helpful for the interpretation of the Raman scattering maps is a comparison with results for the Rayleigh-scattered O vi radiation. Fig. 4 shows Rayleigh scattering maps for the O vi λ1032 radiation in models Xв3 and Xc3 at quadrature phase $\alpha = 90°$. Note that direct (or unscattered) photons from the O vi region are not plotted.

The O vi map for model Xв3 in Fig. 4 shows a photon distribution which traces the cone-shaped surface of the neutral region. This is a result of the high Rayleigh scattering opacity for the O vi λ1032 photons, which prevents the penetration into and escape from deep layers in the giant's neutral wind. From the high UV opacities, we can conclude that the Raman-scattered photons λ6825 are predominately created in the surface layers of the neutral region, which are strongly illuminated by far-UV O vi photons. However, contrary to the Rayleigh-scattered O vi photons, the Raman-scattered photons encounter a much smaller opacity. For the simulations displayed in Figs 3 and 4, the opacity is 285 times smaller for the red Raman-scattered photons when compared to the initial far-UV O vi photons. Thus, once created, a Raman photon may escape in almost any direction through the neutral region apart from an interception by the cool giant.

The UV to red light opacity contrast also accounts for the differences in the O vi Rayleigh and Raman scattering maps of model Xc3. In model Xc3 the scattered radiation at quadrature phase has to penetrate through the outer neutral regions of the giant's wind as in a scattering transmission case. Escape into the sampled direction only occurs for a large fraction of O vi photons after several Rayleigh scatterings, and predominantly from the outer regions in the giant's neutral wind. As a result, the Rayleigh-scattered O vi radiation originates from a very extended region, and traces only weakly the shape of the ionization front (Fig. 4). Contrary to this, the corresponding Raman-scattered O vi, photons escape easily from the central main scattering region (Fig. 3).

4.2   The O vi line radiation

In most models the majority of the emitted O vi line photons undergo no Raman scattering process. They escape
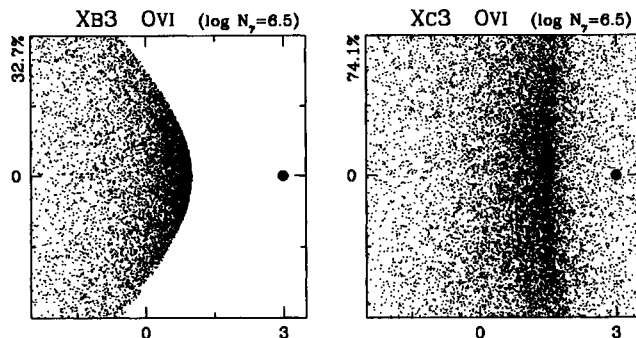
as far-UV photons from the system, either without inter-action or after one or multiple Rayleigh scatterings in the H^0 region.

Fig. 5 gives normalized light curves for the two O vi lines $\lambda\lambda$1032, 1038 for the basic model set Xa3, Xв3, Xc and Xd3. For these light curves all escaping O vi photons have been sampled in bins $N(\alpha)$ as a function of the phase angle α (total bin size 5°) between the binary axis and the line of sight. The photon intensity curve $I(\alpha)$ then follows from the photon number counts per unit solid angle according to $I(\alpha) = N(\alpha)/\sin \alpha$. In principle, the use of finite bins causes a smearing effect which is, however, small (compared to the statistical noise) and negligible for the results presented in this paper.

The intensity curves $I(\alpha)$ in Fig. 5 represent half an eclipse light curve, where the hot component (and the main part of the emission nebula) is in front of the cool component for $\alpha = 0°$ and behind it for $\alpha = 180°$. The O vi line light curves in Fig. 5 are normalized, so that $I_{\lambda 1032}(\alpha) = 1$ and $I_{\lambda 1038}(\alpha) = 0.5$ correspond to the photon intensity emitted by the unobscured nebula. This normalization accounts for the theoretical O vi line emissivity ratio $I_{\lambda 1032}/I_{\lambda 1038} = 2$ under nebular conditions. Statistical errors for the normalized O vi light curves in Fig. 5 are about or less than 0.001.

The O vi line photon budgets for the different models are summarized in Table 2. Table 2 lists the fractions of escaping O vi photons $L_{\lambda 1032}$ and $L_{\lambda 1038}$, of O vi photons which escape after one or several Rayleigh scatterings $S_{\lambda 1032}$ and $S_{\lambda 1038}$, of escaping Raman photons $L_{\lambda 6825}$ and $L_{\lambda 7082}$, and of absorbed photons A.

Table 2 and the O vi line light curves in Fig. 5 show the increasing Rayleigh scattering and absorption effects for systems with more extended and dense H^0 regions. The light curves for models with red giants having lower mass loss rates Xa3 and Xв3 show a relatively weak depression around the eclipse phase $\alpha \approx 180°$, because the cool giant and the associated wind obscures only a small fraction of the very extended nebular O vi line photon source. In these

Figure 4. Maps of the Rayleigh-scattered O vi λ1032 radiation for the models Xв3 and Xc3 at quadrature phase. See text and Fig. 3 for further details.
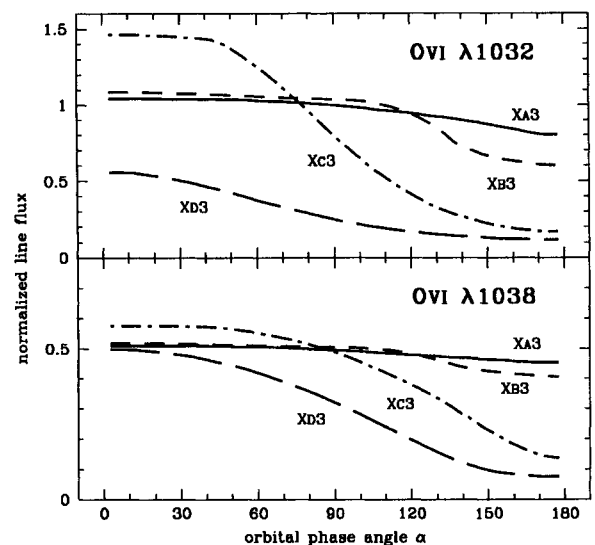

Figure 5. Normalized light curves for the O vi emission lines λ1032 (upper panel) and λ1038 (lower panel) for the basic models Xa3, Xв3, Xc3 and Xd3.

Table 2. Photon budget and quadrature polarization of the Raman process. The columns give the percentages of escaping O VI photons $L_{\lambda1032}$ and $L_{\lambda1038}$, of O VI photons which escape after one or several Rayleigh scatterings $S_{\lambda1032}$ and $S_{\lambda1038}$, of escaping Raman photons $L_{\lambda6825}$ and $L_{\lambda7082}$, and of absorbed photons A. The initially emitted O VI photon luminosity is $L_{\lambda1032}+L_{\lambda6825}+A=100$ per cent and accordingly for the $\lambda1038-\lambda7082$ component. The fraction of O VI escaping without interaction is equal to $L_{\lambda1032}-S_{\lambda1032}$. The table also gives photon budget ratios and the quadrature polarization $p_Q(90°)$ for the Raman-scattered lines. Results are given for the basic model set without modification first, and then for two sets with modifications. The second model set uses a point-like O VI photon source (instead of an extended emission region). The third model set considers only direct escape and the first scattering process. In this case, the fraction of omitted (multiply scattered) photons is 100 per cent $-L_{\lambda1032}-L_{\lambda6825}-A$.

model	budget λ1032 − λ6825				budget λ1038 − λ7082				ratios		pol. $p_Q(90°)$	
	$L_{\lambda6825}$	$L_{\lambda1032}$	$S_{\lambda1032}$	A	$L_{\lambda7082}$	$L_{\lambda1038}$	$S_{\lambda1038}$	A	$\frac{L_{\lambda1032}}{L_{\lambda6825}}$	$\frac{2\cdot L_{\lambda6825}}{L_{\lambda7082}}$	λ6825	λ7082
basic model set												
XA3	1.15	98.07	2.64	.78	.58	98.35	1.05	1.07	85.3	3.99	12.0%	11.6%
XB3	2.08	97.22	4.90	.70	.84	98.25	1.87	.91	46.7	4.95	26.1%	30.9%
XC3	13.65	82.77	25.75	3.58	5.15	90.46	10.64	4.39	6.06	5.30	2.9%	14.6%
XD3	56.69	28.17	24.37	15.14	21.11	61.09	26.07	17.80	.497	5.37	−.76%	2.1%
O VI point source												
XA3	.56	99.05	1.30	.39	.28	99.20	.53	.52	176.	3.91	59.4%	71.9%
XB3	2.55	96.58	5.75	.88	1.05	97.83	2.30	1.12	37.9	4.86	46.2%	62.5%
XC3	14.36	81.85	26.24	3.79	5.42	89.95	11.15	4.63	5.70	5.30	4.0%	18.5%
XD3	56.91	27.85	24.08	15.23	21.22	60.87	25.96	17.91	.489	5.36	−.91%	2.4%
first scattering only												
XA3	.59	97.21	1.77	.35	.37	98.13	.82	.70	166.	3.21	18.5%	14.4%
XB3	1.14	95.65	3.34	.43	.64	97.94	1.56	.73	84.3	3.57	36.6%	35.4%
XC3	6.55	72.54	15.42	2.31	3.81	88.33	8.50	3.83	11.1	3.44	2.0%	13.4%
XD3	14.44	8.62	4.78	6.39	12.15	50.95	15.82	14.09	.597	2.38	−.87%	.67%

models over 90 per cent of the emitted O VI photons escape from the system without any interation. The H^0 region is much more extended in model XC3, so that a larger fraction of photons undergo scatterings and absorption. This produces O VI light curves with a broad and strong eclipse minimum and a significant reflection effect for $\alpha < 60°$. In model XD3 the ionized region is completely surrounded by neutral and relatively dense gas, and the escaping O VI radiation is strongly diminished by Raman scattering and absorption for all escape directions, particularly at large phase angles α.

Some differences are visible between the light curves for the λ1032 and λ1038 lines. These differences are caused by the fact that the λ1032 line photons undergo much more interaction in the H^0 region, due to the 5.2 times larger Rayleigh scattering cross-section and the 2.3 times larger photon-destruction cross-sections $(\sigma_{Ram}+\kappa_{uv})$. Therefore the light curve minima around eclipse, the reflection effect in model XC3, and the absorption in model XD3 are much more pronounced for the λ1032 component. As a result, the O VI line ratio is changed from its initial emission ratio $\Lambda=I_{\lambda1032}/I_{\lambda1038}=2$ to smaller values, $\Lambda < 2$ for phase angles where absorption is important, and to larger values, $\Lambda > 2$ for phase angles where the reflection effect is significant.

The O VI line light curves in Fig. 5 look very similar to the N V and He II Rayleigh scattering line light curves described in Paper II. This is not surprising, as the scattering models are exactly the same, except for the different cross-sections for photon scattering and photon destruction. Paper II gives a detailed description of many different aspects of the Rayleigh scattering effect in symbiotic systems, which also apply to a large extent for the O VI $\lambda\lambda1032$, 1038 line radiation.
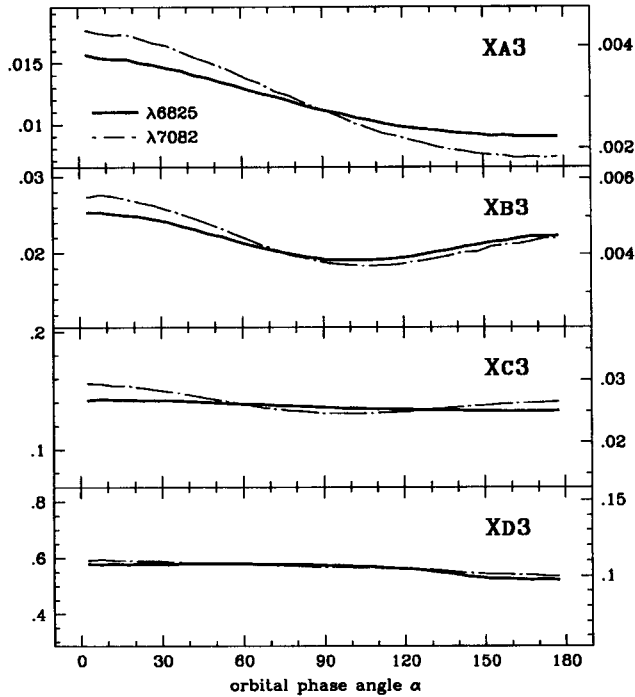
4.3 Light curves for the Raman-scattered lines

Photon light curves for the Raman-scattered O VI emission lines are plotted in Fig. 6 for the models XA3, XB3, XC3 and XD3. The given line photon intensities $I_{\lambda6825}(\alpha)$ and $I_{\lambda7082}(\alpha)$ are again normalized, so that $I_{\lambda1032}(\alpha)=1$ and $I_{\lambda1038}(\alpha)=0.5$ corresponds to the initially emitted O VI photon intensity. Table 2 gives the total photon budgets $L_{\lambda6825}$, $L_{\lambda7082}$ and the corresponding ratios for the two Raman-scattered lines.

In model XA3 the scattering region is confined to a narrow cone surrounding the cool giant and its hemisphere facing the hot component. Only a very small fraction of the emitted O VI photons penetrate into this region and undergo a Raman scattering process. The resulting Raman line intensities are therefore very low. However, $I_{\lambda6825}(\alpha)$ and $I_{\lambda7082}(\alpha)$ show relatively strong orbital variations, because the cool stars occult the main scattering region for large phase angles α. The flux variations are somewhat less pronounced for the λ6825 component. This can be explained by the larger Raman scattering cross-section for the O VI λ1032 component, which is responsible for the production of relatively more Raman photons in regions further out in the giant's wind, which are not subject to varying obscuration.

The Raman line intensities increase rapidly for models having a cool giant with a stronger stellar wind and a more extended scattering region. More extended and dense H^0 regions produce also less pronounced orbital variation in the λ6825 and λ7082 light curves. Obscuration by the cool giant is rather unimportant in the model XB3, and negligible in the models XC3 and XD3.

The orbital variations visible for $I_{\lambda6825}(\alpha)$ and $I_{\lambda7082}(\alpha)$ in model XB3 and for $I_{\lambda7082}(\alpha)$ in model XB3 (less pronounced) are mainly due to the scattering phase function (i.e. Ray-
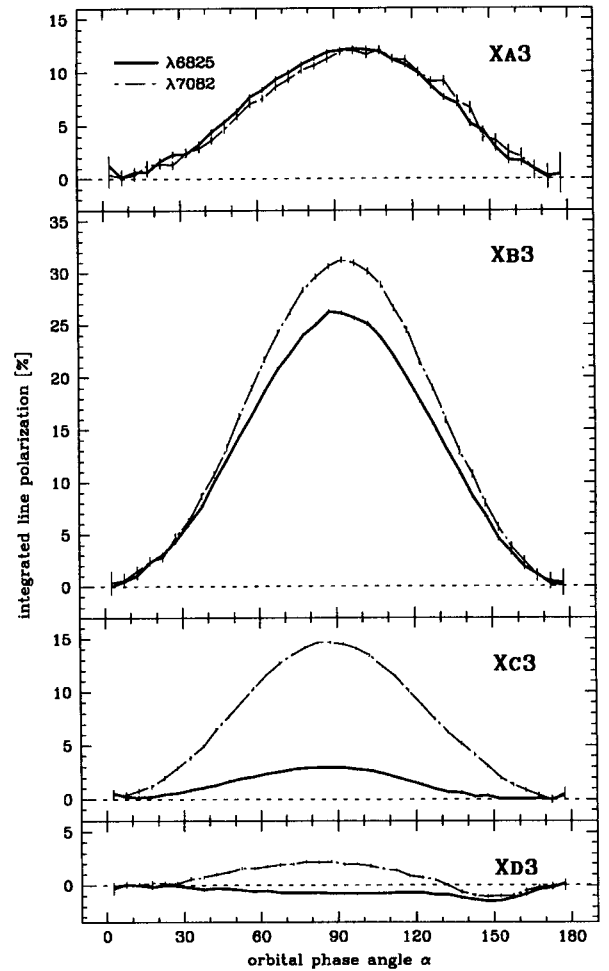
Figure 6. Normalized photon light curves for the Raman-scattered O vi emission lines $\lambda\lambda 6825$, 7082 for the basic model set. The photonintensity scale on the left-hand side refers to the stronger component $I_{\lambda 6825}(\alpha)$ and is normalized relative to $I_{\lambda 1032}(\alpha) = 1$, as emitted by the unobscured O vi nebula. The scale on the right-hand side refers to $I_{\lambda 7082}(\alpha)$ and assumes an initial intensity of $I_{\lambda 1038}(\alpha) = 0.5$. The scalefactor between the two scales is equal to the ratio of escaping Raman-scattered photons $2 \times L_{\lambda 6825}/L_{\lambda 7082}$ as given in Table 2. For all panels the upper plot limit is three times the lower limit.

Figure 7. Integrated line polarization $p_Q(\alpha)$ of the Raman-scattered O vi emission lines $\lambda\lambda 6825$, 7082 as a function of the orbital phase angle α for the basic models X$_A$3, X$_B$3, X$_C$3 and X$_D$3. The polarization is given as normalized Stokes parameter $p_Q = Q/I$ and expressed as a percentage.

leigh scattering phase function) of the Raman scattering process. This phase function prefers backward and forward scattering. Therefore we see in these light curves a backward scattering maximum at $\alpha = 0°$, a forward scattering maximum at $\alpha = 180°$ which is somewhat weakened by obscuration, and a minimum around $\alpha = 90°$ for perpendicular scatterings.

This phase function effect in the light curves requires that most $\lambda 6825$ or $\lambda 7082$ photons originate from a direct Raman scattering process, with a well-defined general propagation direction for the initial O vi photons. These requirements are not well fulfilled for systems with more extended and dense H^0 regions, like X$_C$3 or especially X$_D$3. In these models Raman scattering may occur for O vi photons being released in (almost) any direction. In addition, a substantial fraction of O vi photons undergo first one or more Rayleigh scatterings before a Raman scattering process takes place.

Obscuration by the red giant is less important for the Raman line light curves in the models X$_C$3 and X$_D$3. This is due to the very large size of the scattering regions when compared to the red giant. However, higher absorption opacities $\kappa_{\rm red}$ would produce substantial Raman line flux variations due to obscuration by the cool giant's wind.

The light curves for the Raman-scattered emission lines differ in many respects from the O vi line light curves presented above (Fig. 5) or other Rayleigh scattering light

curves described in Paper II. This qualitative difference is mainly due to the fact that the $\lambda\lambda 6825$, 7082 features consist only of scattered light. The Raman-scattered radiation is not diluted by direct radiation from a photon source, which is in the case of Rayleigh scattering often the dominating component of the escaping radiation.

4.4 Integrated line polarization

The scattering polarization in the Raman lines depends on various parameters of the scattering geometry, such as the general orientation of the system, the extent of the scattering region and the photon source, or the fraction of multiply scattered photons. These strong dependencies are apparent in Fig. 7, where the integrated line polarization is plotted as funtion of the phase angle α. The polarization is given as normalized Stokes parameter $p_Q(\alpha) = Q(\alpha)/I(\alpha)$, and expressed as a percentage. Positive p_Q-values stand for a polarization perpendicular to the binary axis (the line connecting both stars), while the polarization direction is parallel for negative p_Q-values. Error bars indicate the statistical

errors for p_Q, which are calculated according to $\sigma_p = [(1 - p^2)/I]^{1/2}$ (Paper I, section 4.3). The Stokes U polarization components cancel due to the rotational symmetry of the scattering models.

The polarization light curves for the models XA3, XB3 and XC3 show a pronounced maximum around quadrature phase $\alpha \approx 90°$ and only little polarization near the conjunction phases $\alpha \approx 0°$ and $180°$. This behaviour reflects the dipole-type phase matrix (Rayleigh phase matrix) of the Raman scattering process. According to this phase matrix fully (100 per cent) polarized light results for radiation which undergoes a single scattering process with a scattering angle of $\theta_s = 90°$, while no polarization is produced for the forward and backward scattering directions. In our models the maximum polarization around quadrature phase, expressed as $p_Q(90°)$, reaches values which are much lower than 100 per cent (see also Table 2). This reduction of the scattering polarization is mainly due to geometric compensation, and to a lesser extent also due to multiple scatterings. These effects can be assessed quantitatively in Table 2, where results are given for models with an extended photon source (basic models), for models with a point source, and for models which omit multiple scatterings.

In model XA3 the nebular photon source surrounds the scattering region on one side. This causes a strong geometric compensation effect, and it results a relative low net polarization $p_Q(90°) = 12$ per cent. The polarization would be about $p_Q(90°) = 60$ per cent (for $\lambda6825$) for a model with the same scattering region but an O VI point source at the position of the hot component (see Table 2). A higher polarization is not reached because multiple scatterings, which occur predominantly in and near the atmosphere of the cool giant, produce a substantial fraction of unpolarized Raman-scattered light (see Paper I).

The model geometry XB3 has a more pronounced scattering asymmetry, with a clear separation of the photon source on the side of the hot component and the scattering region on the side of the cool giant. Therefore geometric compensation is less important, and it results a relatively high net polarization which is substantially larger than in the other models. The polarization light curves of model XB3 show a difference between the $\lambda6825$ and $\lambda7082$ components. At quadrature phase the polarization reaches $p_Q(90°) = 31$ per cent for the weaker $\lambda7082$ line, but only $p_Q(90°) = 26$ per cent for the stronger $\lambda6825$ line. This difference can be explained as a multiple-scattering effect. The larger Rayleigh scattering cross-sections for the $\lambda1032$ component makes it more likely that for these photons one or multiple Rayleigh scatterings occur before a conversion into a Raman $\lambda6825$ photon takes place. These multiple scatterings tend to decrease the net polarization in the Raman line. The fraction of multiply scattered Raman photons is 45 per cent in the $\lambda6825$ component, but only 24 per cent in the $\lambda7082$ component. If we consider only the directly scattered photons, then the quadrature polarization is about 36 per cent for both Raman lines (see Table 2).

In model XC3 the O VI photon source is largely surrounded by the scattering region, and the associated geometric compensation significantly lowers the integrated polarization in the Raman lines. The geometric compensation nearly nullifies the net polarization in the $\lambda6825$ component, which has only a quadrature polarization of

$p_Q(90°) = 2.9$ per cent. In this special case the perpendicular polarization contribution (perpendicular to the binary axis) from scatterings near the cool component is almost compensated by the parallel polarization contribution from scatterings in the outer wind regions above and below the binary axis. A relatively small variation in the H^0 density, or in the mass-loss rate of the cool giant, changes significantly the weight of these two scattering regions and therefore the resulting line polarization (see Section 4.6.1). The Raman line $\lambda7082$ in model XC3 shows a much higher polarization $p_Q(90°) = 14.5$ per cent than the $\lambda6825$ component. This is a result of the much smaller scattering cross-sections for the O VI $\lambda1038$ photons. Scatterings in the outer wind region are less likely for this component, so that the perpendicular polarization component form near the cool giant dominates. In model XC3, multiple scatterings have only a minor effect on the integrated polarization in the Raman lines when compared to the geometric cancellation of the polarization signal.

The H^0 region completely surrounds the O VI photon source in model XD3. Therefore the scattering geometry is not too far from spherical symmetry, and geometric compensation is close to perfect. In addition, a large fraction of escaping Raman photons undergo first one or more Rayleigh scatterings in the H^0 region. These two properties explain why only a small integrated line polarization is obtained for both Raman lines in this model. The polarization curves $p_Q(\alpha)$ for model XD3 show for $\alpha > 135°$ an enhanced negative polarization. This is due to obscuration of the 'central' scattering region between the two stellar components by (the inner part of) the cool giant's wind. Although the occulted region is relatively small, it is the main contributor of positively or perpendicularly polarized Raman photons.
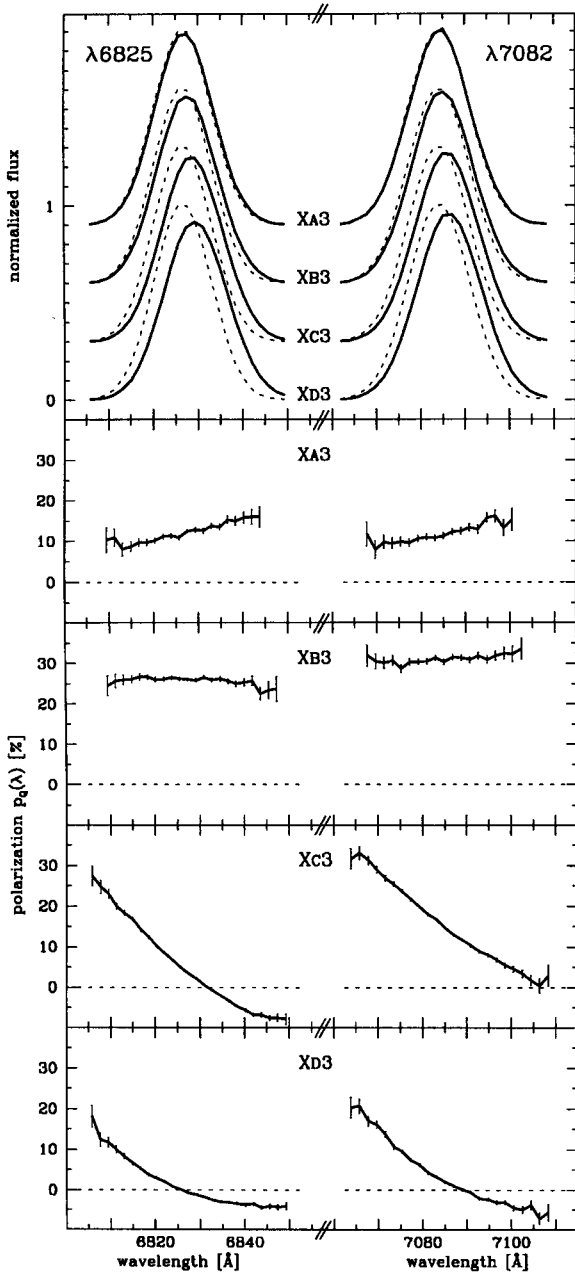
4.5 Spectropolarimetric structure in the Raman lines

With the present Monte Carlo simulations we can also model the spectroscopic and spectropolarimetric structure of the Raman-scattered lines, which provide additional information on the system geometry. The scattering polarization reflects the scattering geometry, while the Doppler shifts introduced by the scattering particles distinguish regions with different systematic gas motions.

Fig. 8 shows the calculated spectropolarimetric structures of the Raman-scattered O VI lines at quadrature phase ($\alpha = 90°$) for the basic model set. The total bin width for the sampled photons is $\Delta\alpha = 10°$. The initial O VI radiation has a Gaussian line structure centred on the rest wavelengths of the O VI transitions, and a velocity width of $\Delta v_D = 100$ km s^{-1}. The $\lambda6825$ and $\lambda7082$ intensity profiles are flux-normalized. The dotted curves give for comparison the Gaussian profile which would result if Doppler shifts are neglected.

For the interpretation of the calculated line profiles we recall that Doppler shifts $\Delta\lambda/\lambda$ due to the motion of the scattering H^0 atom relative to the incoming photon are multiplied by a factor of about 6.7 in the Raman scattering process (Section 3.2.3). This effect tends to produce line profiles where blue-wing photons received a Doppler shift in the Raman process by approaching H^0 scatterers with respect to the O VI photon source, while the red-wing photons are Raman-scattered by receding H^0 atoms. For a

Figure 8. Intensity (top panel) and polarization structure $p_Q(\lambda) = Q(\lambda)/I(\lambda)$ for the Raman-scattered emission lines at quadrature phase ($\alpha = 90°$) for the basic models X_A3, X_B3, X_C3 and X_D3. The intensity profiles are flux-normalized. The dotted curves in the top panel give for comparison the Gaussian profile which would result if Doppler shifts are neglected. The error bars for p_Q account for the photon statistics.

the Raman line $\lambda6825$ is shifted by the Doppler effect by 0.4 Å in model X_A3, 1.0 Å in X_B3, 2.1 Å in X_C3, and 2.9 Å in X_D3. The systematic redshift is small in model X_A3, because about equal numbers of Raman photons are produced in the approaching and receding parts of the red giant's wind (with respect to the O VI source). For models X_B3, X_C3 and X_D3 the neutral region with receding H^0 scatterers increases progressively, while the size of the region with approaching H^0 scatterers is not significantly changed.

The polarization profiles are plotted as normalized Stokes parameter $p_Q = Q_{90°}(\lambda)/I_{90°}(\lambda)$ and expressed as percentages. Positive p_Q-values stand for polarizations perpendicular to the binary axis, while the polarization direction is parallel to the binary axis for negative p_Q-values. The statistical errors in p_Q are indicated as error bars. The errors are large in the line wings, where the photon flux goes to zero.

The polarization structure in the Raman lines mirrors the geometry of the scattering regions with different particle motions relative to the O VI source. The polarization in the blue line wing is produced in the central scattering region, between the two stars, where the scatterers move towards the hot component. This region is illuminated by O VI photons mainly along the binary axis. The polarization direction in the blue line wing (blueshifted Raman photons) in all models is therefore perpendicular to the binary axis. For the polarization in the red line wing we have to consider two cases. In models X_A3 and X_B3 the region with receding scatterers is confined to the cool component's side. Scatterings in this region produce a polarization perpendicular to the binary axis or perpendicular to the general direction of illumination. The models X_C3 and X_D3 have much more extended scattering regions. Therefore a large fraction of O VI photons with directions away from the binary axis (roughly perpendicular) undergo Raman scatterings with receding atoms in the 'outer' wind region. This will produce red line wing photons with negative polarization or a polarization parallel to the binary axis. As a result, the polarization in the Raman lines show a strong gradient, from the blue line wing with a strong perpendicular (positive) polarization towards a parallel (negative) polarization in the red line wing. The strength of the perpendicular and parallel polarization components depends thereby on the relative weight of the different scattering regions.

The relative structure in the Raman lines depends only slightly on the phase angle α. Fig. 9 shows, as an example, the spectroscopic and spectropolarimetric profiles for the $\lambda6825$ component for the model X_C3 at different phase angles. Strong changes as a function of α are visible in the total line polarization (see also Fig. 7), but not in the (relative) spectropolarimetric line structure. This is another manifestation of two main properties of the considered O VI Raman scattering effect, namely that the scattering region is almost transparent for the once produced Raman photons, and that the introduced Doppler shifts are almost independent of the escape direction. Thus we see from all directions the same scattering region and the same Doppler shifts. The Raman lines in the models X_A3 and X_B3 behave similarly. In model X_D3, subtantial obscuration of the central scattering region by the cool giant's wind occurs for $\alpha > 135°$ (see Section 4.3). As a result, the perpendicular polarization

spherically symmetric cool giant's wind, the blueshifted Raman photons must therefore be produced in that part which faces and moves toward the O VI line photon source. In all our models this region lies in the neutral zone between the two stellar components. Accordingly, the redshifted Raman photons originate in the 'outer' neutral wind region.
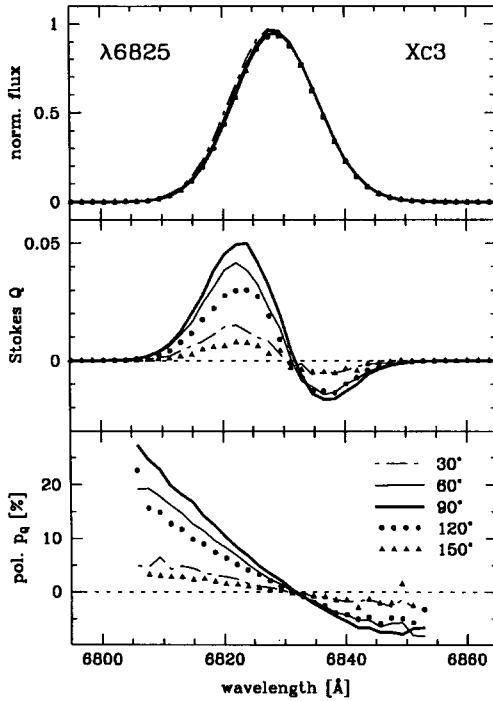
The intensity profiles of the Raman-scattered lines show a systematic redshift, which is larger for models with a more extended neutral scattering region. The mean wavelength of
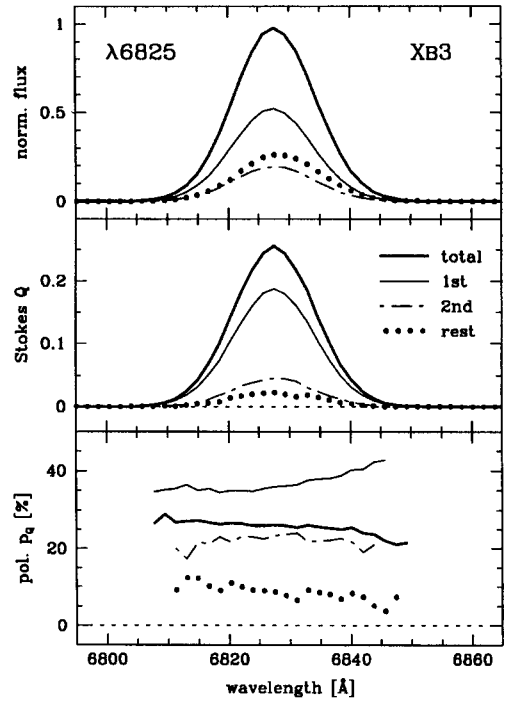
Figure 9. $I(\lambda)$, $Q(\lambda)$ and $p_Q(\lambda) = Q(\lambda)/I(\lambda)$ for the Raman-scattered emission line $\lambda 6825$ in model $X_C 3$ and different phase angles α.

Figure 10. Contributions to the total $\lambda 6825$ line of Raman photons produced in the first scattering process, in the second scattering process after one Rayleigh scattering, and of Raman photons produced after two or more Rayleigh scatterings (rest). $I(\lambda)$, $Q(\lambda)$ and $p_Q(\lambda) = Q(\lambda)/I(\lambda)$ of the different contributions are given for model $X_B 3$ at phase angle $\alpha = 90°$.

component in the blue line wing, which is present for smaller phase angles (e.g., at 90° as in Fig. 8), disappears completely for $\alpha > 135°$.
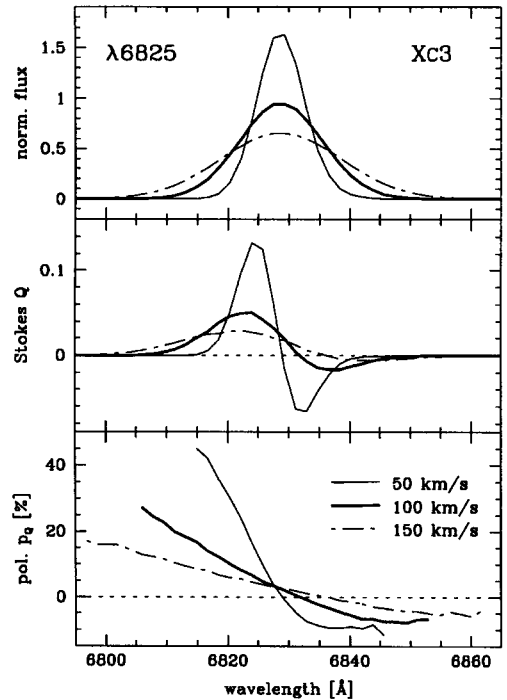
Effects like geometric compensation, multiple scatterings, wind velocities, O VI photon source geometry and others are also important for the finer details of the resulting polarization structure in the Raman lines. The following discussion is not exhaustive, and describes only some of these effects.

The contributions of direct scatterings and multiple scatterings to the resulting O VI Raman lines is shown in Fig. 10 for model $X_B 3$. In this model, 55 per cent of the escaping $\lambda 6825$ line photons are produced in the first scattering process (directly scattered Raman photons), 20 per cent are produced in the second scattering process after one initial O VI Rayleigh scattering, and the rest are produced after two or more Rayleigh scatterings. Fig. 10 shows that the escaping radiation from direct scatterings has a much higher polarization than the radiation escaping after multiple scatterings. This is expected, as Rayleigh scatterings in the H^0 region tend to dilute the strong anisotropy of the O VI radiation field and subsequently the resulting scattering polarization.

The spectropolarimetric structures of the Raman lines with a strong polarization gradient are very sensitive to changes in the width of the initial O VI line, or to changes in the velocity field of the scatterers. Fig. 11 shows, as an example, the $\lambda 6825$ line in model $X_C 3$ for different widths Δv_D of the initial O VI line. It is clearly visible that the perpendicular and parallel polarization components reach more extreme polarization values Q and p_Q for narrow O VI lines. This is the case, because the Doppler shifts introduced

Figure 11. Dependence of the spectropolarimetric profile on the linewidth Δv_D (FWHM) of the initial O VI $\lambda 1032$ line of the Raman line $\lambda 6825$ in model $X_C 3$ (at $\alpha = 90°$).

in the Raman process by the moving H^0 particles are relatively large compared to the O VI linewidth. The two polarization components tend to merge for O VI lines with a larger width, and it results in a polarization structure which is smoothed down. The same effects would result for a fixed O VI linewidth but different Doppler shifts as a result of higher or lower velocities in the red giant's neutral wind.

4.6 Models with different system parameters

4.6.1 *Other combinations of X_{H^+} and $\dot{M}_x$*

In the basic model set X_A3, X_B3, X_C3, X_D3, the shapes of the ionization front are locked to the mass-loss rate of the cool giant $\dot{M}_x$ (see Table 1). Thus, within the basic model set, a higher mass-loss rate for the cool giant $\dot{M}_x$ implies a more closed and compact ionization region. Fig. 12 gives results for models, where $\dot{M}_x$ for a given geometry is a factor 3.16 lower (models X_A2, X_B2, X_C2, X_D2) or a factor 3.16 higher (models X_A4, X_B4, X_C4, X_D4). We recall that the small capital in the model name defines the X_{H^+}-parameter for the shape of the ionization front. The number in the third digit gives, as described in Paper II, the luminosity of the hot

Figure 12. Comparison of model results for the geometries X_A, X_B, X_C, X_D with three different values for the mass-loss rate of the cool giant $\dot{M}_x$. For each model the values for five phase angles $\alpha = 30°$, $60°$, $90°$, $120°$ and $150°$ are plotted as indicated in the bottom panel for model X_B3. The top panel gives normalized photon line fluxes for O VI $\lambda1032$ and the Raman line $\lambda6825$ (bold symbols). The photon flux ratios $I(\lambda1032)/I(\lambda6825)$ are given in the middle panel, and the integrated Raman line polarization $p_Q(\lambda6825)$ in the bottom panel.

component L_x for a given scaling factor x [e.g., 2 for log $(L_x/L_\odot) = 2 + \log x$]. This also defines the mass-loss rate of the cool giant $\dot{M}_x$.

The top panel in Fig. 12 shows that, as expected, the production of Raman-scattered O VI $\lambda6825$ photons is increased for more extended and dense neutral scattering regions. For a given model geometry the relative Raman line flux is about a factor 3.5 ± 1.0 higher for the X_A4, X_B4, X_C4, X_D4 models when compared to the corresponding X_A2, X_B2, X_C2, X_D2 models. The enhanced density enlarges the size of that part of the neutral scattering region, where incoming O VI photons have a high probability of being converted to Raman photons.

Emissivities for the O VI $\lambda1032$ line are also plotted. The main effects of an enhanced H^0 density on the escaping O VI radiation are a more pronounced eclipse minimum for the model geometries X_B and X_C, a stronger reflection effect for X_C, and substantially more absorption in model geometry X_D.

Photon flux ratios between the direct $\lambda1032$ and Raman-scattered $\lambda6825$ O VI lines are plotted in the middle panel of Fig. 12. This presentation of model results may be more helpful for the interpretation of observational data.
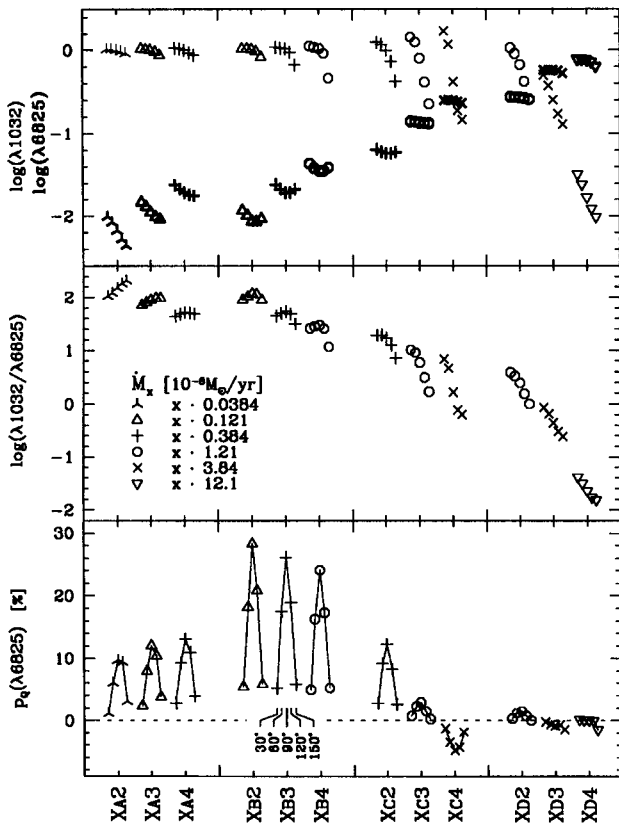
The results for the integrated polarization in the Raman-scattered line $\lambda6825$ are plotted in the bottom panel of Fig. 12. For the model geometries X_A and X_B the line polarization $p_Q(\lambda6825)$ depends only slightly on the density in the scattering region. For these models a change of the H^0 density in the neutral wind region invokes no qualitative difference in the general scattering pattern of the system.

Contrary to this, the polarization $p_Q(\lambda6825)$ in the models X_C reacts in an extremely sensitive way to a change in the H^0 density. This is a result of the X_C model geometry, where the perpendicular polarization contribution from scatterings near the cool component balances almost the parallel polarization contribution from scatterings in the outer wind region above and below the binary axis. A relatively small variation in the mass-loss rate of the cool giant significantly changes the weight of these two scattering regions, with a correspondingly strong effect on the integrated line polarization $p_Q(\lambda6825)$. Also the $\lambda6825$ line polarization structure in the model geometry X_C is extremely sensitive to any change in the H^0 density in the scattering region. This is shown in Fig. 13, where the polarization structure of the Raman line $\lambda6825$ at $\alpha = 90°$ is plotted for the models X_C2, X_C3 and X_C4.

In model geometry X_D the H^0 region surrounds the O VI photon source. Therefore the polarization goes rapidly to zero for higher H^0 densities, as the scattering region becomes more and more opaque for all directions.

4.6.2 *Dependence on the absorption cross-sections*

All previous model calculations in this paper used the 'standard' absorption cross-sections $\kappa_{uv} = 1.0 \times 10^{-24}$ cm^{-2} H^{-1} for the far-UV O VI photons, and $\kappa_{red} = 0.1 \times 10^{-24}$ cm^{-2} H^{-1} for the Raman-scattered photons. However, the opacities would be significantly higher if dust particles are present in the neutral wind of the red giant. In this section we explore the dependence of κ_{uv} and κ_{red} with a small grid of simulations for model X_C3. The results are summarized in Fig. 14.

Fig. 14 shows that the O vi eclispe minima are more pronounced for larger κ_{uv}-values. A further expected result is that the Raman line emissivities decrease with increasing absorption cross-sections κ_{uv} and κ_{red}.
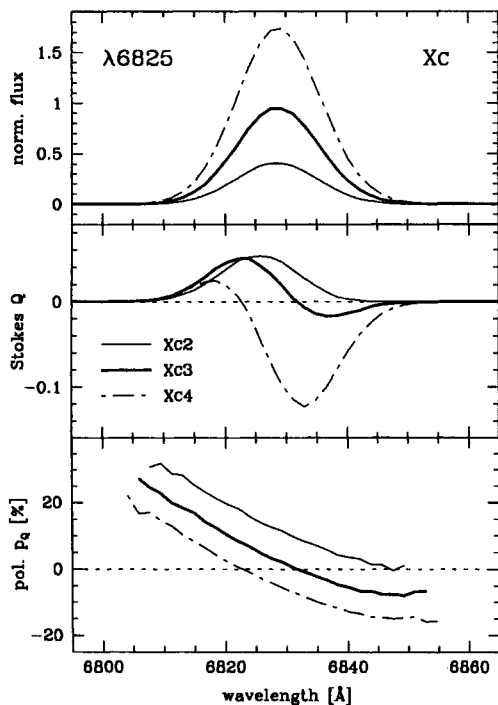
The strong κ-dependent changes of the integrated line polarization p_Q in the Raman-scattered lines are interesting. The general trend is that the positive (perpendicular) polarization component in the Raman lines suffers relatively more attenuation for larger absorption cross-sections.

An increased κ_{red}-value (for given κ_{uv}) suppresses the escape probability of the Raman-scattered photons. This predominantly affects the positive polarized Raman photons from the innermost scattering region between the two stellar components. This absorption is phase-dependent and strongest for large α when the escape column density is highest. This also produces an enhanced α-dependence in the Raman line emissivities. Escape from the outer scattering region which produces the negative polarization component is much less affected by an increased κ_{red}-value.
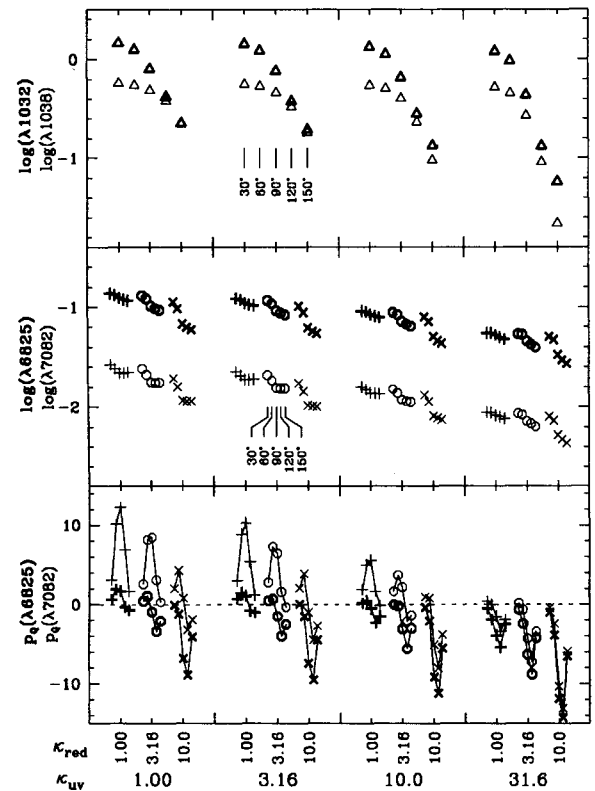
A similar differential dependence between the 'inner' and 'outer' scattering regions also exists in relation to the far-UV absorption cross-section κ_{uv}. The probability for the production of a Raman photon from an O vi photon in the 'inner' scattering region behaves like $\sigma_{Ram}/\kappa_{tot}$, where κ_{tot} stands for the sum of all UV-scattering and absorption cross-sections. This relation holds if the O vi photon escape opacity is large ($\tau_E \rightarrow \infty$). Contrary to this, photon escape is frequent in the 'outer' scattering region, and the Raman

photon production depends less on an increased value of κ_{uv} or κ_{tot}. In the extreme case $\tau_E \ll 1$, the probability for Raman scattering is given by $\sigma_{Ram}d_E$ (d_E is the escape column density), which is largely independent of the absorption cross-section. Thus an enhanced κ_{uv} more efficiently suppresses the production of Raman photons in the dense 'inner' scattering region and therefore the positive polarization component in the Raman line.

A most remarkable result in Fig. 14 is that the large discrepancies in the line polarization between the $\lambda6825$ and $\lambda7082$ components disappear for large κ_{uv}. The explanation is that a large absorption cross-section reduces the high opacity contrast between the two components, which is due to the strong wavelength dependency of the Rayleigh and Raman scattering cross-sections. A small opacity contrast between the two O vi components makes the relative O vi intensity field in the scattering region similar for both lines. As a result, both Raman-scattered lines originate from the same region, and their polarization signals are similar.

Figure 14. Comparison of results from model Xc3 using different absorption cross-sections κ_{uv} and κ_{red} (given in 10^{-24} cm^2 H^{-1}). The top panel gives line photon intensities for O vi $\lambda1032$ (bold symbols) and $\lambda1038$, and the middle panel the corresponding values for the Raman-scattered lines $\lambda6825$ (bold) and $\lambda7082$. The integrated Raman line polarization $p_Q(\lambda6825)$ (bold) and $p_Q(\lambda7082)$ are given in the bottom panel. Line photon intensities are normalized as in Figs 5 and 6. The O vi results do not depend on κ_{red}, and are therefore given only once for a given κ_{uv}. For each model the values for five phase angles $\alpha=30°$, $60°$, $90°$, $120°$ and $150°$ are plotted as indicated in the top and middle panels. The points in the bottom panel are connected by straight lines for clarity.

Figure 13. Dependence of the spectropolarimetric profiles on $\dot{M}_x$ or the H^0 density in the scattering region for the Raman line $\lambda6825$ in model geometry Xc ($\alpha=90°$). Compared to $\dot{M}_x=x \times 1.21 \times 10^{-6}$ M$_\odot$ yr^{-1} in model Xc3, the mass-loss rate $\dot{M}_x$ is a factor 3.16 higher in model Xc4 and a factor 3.16 lower in model Xc2.

5   DISCUSSION

In this section, a comparison is made between the results of the Monte Carlo simulations presented in Section 4 and the existing observations as summarized in Section 2. Such a comparison between simulations and observations should clarify where the models agree with the observations and where they disagree. This forms a guide for future theoretical and observational investigations. In the third subsection, we summarize the constraints on the scattering geometry in symbiotic systems. This discussion is based on the findings of the present simulations of the Raman-scattered lines and the simulations of the Rayleigh scattering effects in Paper II. The last subsection compares the findings of this paper with the X_{H^+}-parameter determination of Mürset et al. (1991).

5.1   Agreements between model results and observations

The aim of the present model simulations is to examine the basic properties of the Raman-scattering problem in symbiotic systems. Thereby the emphasis is put on the exploration of the vast and poorly known model parameter space for symbiotic systems. No attempt is made to simulate the observations of a particular object. The comparison between simulations and observations is therefore more of a general nature.

We first note that our models for symbiotic systems can produce strong Raman-scattered O VI $\lambda\lambda 6825$, 7082 emission lines. This is not an obvious result, as Raman-scattered O VI lines have up to now been observed only in symbiotic systems. The cross-sections for Raman scattering are small, and special conditions are required for the process to be observable. The present simulations, which are based on a widely accepted model for the ionization geometry of symbiotic systems, produce a substantial amount of Raman-scattered photons.

A quantitative comparison between the observed and calculated flux in the Raman-scattered lines is best made via the photon ratio $F(\lambda 1032)/F(\lambda 6825)$. The few existing (preliminary) results from O VI $\lambda\lambda 1032$, 1038 observations suggest photon ratios in the range 5–50. Such values are typical for model geometries X_B and X_C (see Table 2 and Fig. 12).

The simulations give for most models a Raman line ratio in the range $F(\lambda 6825)/F(\lambda 7082) = 4$–5.5, in good agreement with the observations.

The fluxes of the Raman-scattered lines show no strong orbital variations in the models presented. Good time-series of $\lambda 6825$ flux measurements are very scarce, but the existing observations support the low amplitude in the calculated flux variations (e.g. Schmutz et al. 1994). There exist to our knowledge no observations which show a substantial occultation of the $\lambda\lambda 6825$, 7082 emission region by the cool giant. This implies that the neutral scattering region is substantially larger than the cool giant.

Scattering in the expanding wind of the red giant produces a systematic redshift of the mean wavelengths in the Raman-scattered lines. This redshift depends on the wind velocity of the red giant and the extent of the neutral scattering region. The mean redshifts are about 1–3 Å in our models. This explains at least partly the systematic redshift

of about 4–5 Å observed in the Raman-scattered lines. The remaining wavelength discrepancy may be explained by a systematic redshift of the initial O VI resonance line due to P Cygni-like radiative transfer effects (see Schmid 1989).

The spectropolarimetric data obtained so far revealed for the Raman-scattered lines an integrated polarization of about 6 per cent on average and maximum values above 10 per cent. Such values are obtained in the simulations for model geometries X_A and X_C. It should be noted that very high polarization values in the range 20–30 per cent, as obtained in the models X_B, have not been reported (see next section).

The adopted scattering model for symbiotic systems implies that the polarization in the Raman-scattered emission lines changes periodically due to the binary motion. Such variations in the percentage polarization as well as in the polarization direction have been detected for symbiotic systems.

Different types of polarization structures have been observed in the Raman-scattered emission lines. The presented simulations reproduce various general properties of the spectropolarimetric line structure. Schmid & Schild (1994) distinguished between three types of observed profiles. Type I profiles show constant polarization through the line as in model X_B3. Type II profiles show a decreasing polarization from the blue line wing to the red line wing, with no polarization angle change. Such profiles resulted in the simulations for model X_C2 ($\lambda 6825$) or model X_C3 ($\lambda 7082$). The type III profiles with a polarization angle flip are, for example, obtained in model X_C3 ($\lambda 6825$) or in model X_D3. The observational data suggest that type III profiles may occur predominantly in systems with red giants undergoing strong mass-loss. This correlation is supported by the Monte Carlo simulation, where only models with high mass-loss rates and extended scattering regions (e.g., X_C3 and X_D3) give polarization profiles with positive and negative (perpendicular and parallel) polarization components.

5.2   Disagreements

The present simulations are based on simplified models of symbiotic systems, in order to reduce the computational effort. It is clear that some of the introduced simplifications cause disagreements between the simulations and observations. Some of the emerging differences have therefore been expected to occur or suspected of occurring beforehand, while others have only been revealed by the actual model simulations.

A major shortcoming of the present simulations is the rotational symmetry of the scattering models. Geometric compensation in a rotationally symmetric system produces polarization signals with two polarization directions at most – perpendicular and parallel. The presented models can therefore not reproduce all those Raman-scattered emission lines, which show a range of polarization angles. These lines are produced in symbiotic systems with a scattering geometry which deviates substantially from a rotational symmetry. The surveys of Schmid & Schild (1994) and Harries & Howarth (1996b) show that at least a third of all symbiotic systems with Raman lines have more than just two polarization directions perpendicular to each other. For all

these systems a rotationally symmetric scattering geometry is not adequate, except as a preliminary approximation. Schild & Schmid (1996) discuss this problem in more detail, and suggest a simple model for a three-dimensional scattering geometry for the system V1016 Cyg.

Spectroscopic observations of the Raman-scattered emission lines of symbiotic systems show in most cases highly structured intensity profiles with two or more intensity peaks (e.g. Allen 1980; Harries & Howarth 1996b). The corresponding spectropolarimetric data show also often two or three peaks in the percentage polarization as well as in the polarized flux. These strong spectroscopic and polarimetric line structures are not obtained in the present simulations. These discrepancies may probably be associated with the adopted initial O VI line structure, which was assumed to be Gaussian and location-independent. This simplification neglects gas flows and radiative transfer effects in the nebular O VI zone. An alternative explanation is that the velocity structure in the neutral wind of the cool giant differs in symbiotic systems significantly from a slow $(v_\infty < 30$ km s$^{-1})$, spherically symmetric outflow.

For some symbiotic systems there are good spectropolarimetric observations of both Raman lines available. In at least most of these observations, there is no qualitative difference in the spectropolarimetric line structure present. Contrary to this, the simulations for model geometry XC3 and XD3 show large discrepancies between the $\lambda 6825$ and $\lambda 7082$ components in both the integrated line polarization and in the spectropolarimetric line structure. In Section 4.6.2, it was shown that this discrepancy disappears in model XC3, if strong absorption of O VI photons in the far UV is assumed. Very strong absorption in the UV could be explained by dust particles in the neutral wind of the cool giant. This seems to be a plausible explanation for the dusty or D-type symbiotic systems which should be further investigated.

The simulations for model geometry XB3 give very high values for the integrated polarization (up to 30 per cent) in the Raman lines. Such values have hitherto not been reported. This suggests that the geometric compensation of the polarization signal is too small in model XB3. The geometric compensation effect would be larger if the neutral scattering region or the nebular O VI region is more extended. In the latter case, the O VI zone must have a similar cone shape to the neutral scattering region (as in model XA3; see Fig. 2). The assumption that symbiotic systems have more extended neutral regions than in model XB3 would imply that large X-parameters, $X_{H^+} \gtrsim 4$, are not appropriate for symbiotic systems.

5.3 On the likely scattering model for symbiotic systems

The geometry of symbiotic systems is explored in this paper by simulations of the Raman-scattered emission lines. This study is complemented by the previous simulations of the Rayleigh scattering effects (Paper II). Together they form a comprehensive computational investigation of the H^0-scattering processes in symbiotic systems. A critical comparison of model results and observational data from both studies now provides new constraints on the likely scattering geometry in symbiotic systems.

We compare the results from the different model simulations with the 'average' or 'typical' behaviour in observed systems. Of course, it is dangerous to introduce an 'average' behaviour for such a heterogeneous group of objects as the symbiotic systems. However, it would be too involved to discuss all the specialities of individual objects. Therefore it must be noted that such a more general but superficial view is biased towards systems where the Rayleigh or Raman scattering effects are well observed. This means that for the discussion on Rayleigh scattering only systems with well-observed eclipses are considered, like EG And, SY Mus, BF Cyg, HBV 475 and a few others. There exists practically no information on Rayleigh scattering in non-eclipsing systems or in D-type systems. Similarly, the discussion on Raman scattering properties holds only for symbiotic stars, which show the Raman-scattered O VI lines.

Keeping these limitations in mind, we compare here the computational results for the different model geometries A3, B3, C3 and D3 with these 'average' observations. It is recalled that the model parameters for the X-series in this paper are identical to the S-series in Paper II.

The models in Paper II calculate the effects of Rayleigh scattering in the atmosphere and wind of the cool giant. The simulations provide eclipse light curves for the far-UV continuum of the hot component at $\lambda\lambda 1250$, 1350 and 1700, light curves for the nebular emission lines N v $\lambda 1240$ and He II $\lambda 1640$, and the phase-dependent spectral changes in the hot continuum radiation.

In Paper II, the best match between simulations and observations is obtained with the Rayleigh scattering simulations SB3. The continuum eclipse light curves and the corresponding spectral changes match the 'average' eclipse observations quite well, although the eclipse duration may be somewhat too short in model SB3. The emission-line light curves of model SB3 show orbital variation which are, however, far less pronounced than in the observations. It is argued that this problem may partly be solved by adjusting the nebular geometry, and also by enhancing the far-UV absorption opacity. A better agreement with the observed emission-line light curves is obtained with the Rayleigh scattering model SC3, which has a much more extended neutral scattering region. However, in model SC3, the calculated continuum light curves and spectra show far too strong a reflection effect. Again adjustment of the absorption opacity may improve, but probably not resolve, this situation. Less agreement is achieved with other models. The model SA3 gives a very short eclipse phase and is not able to produce significant emission-line variations. For model SD3, the resulting light curves and spectral properties are not observed in eclipsing symbiotic systems.

According to the results of this paper, the best Raman-scattering model is XC3. It produces Raman lines, having about the right strengths [i.e., $F(\lambda 1032)/F(\lambda 6825)$ ratio], somewhat low but reasonable percentage polarizations, and spectropolarimetric line structures which are in general agreement with the observations. A problem is the overall difference in the polarization signal between the $\lambda 6825$ and $\lambda 7082$ components. This may be resolved by adjusting the absorption cross-sections κ_{uv} and κ_{red}, as described in Section 4.6.2. However, in this case the polarization signal for the 'best' XC model would be too small (i.e., negative).

© 1996 RAS, MNRAS **282**, 511–529

Model $X_{B}3$, with its smaller scattering region, produces much stronger polarization signals than $X_{C}3$, but they substantially overshoot the observed values for the integrated polarization in the Raman lines. Line strengths and spectropolarimetric line structures in model $X_{B}3$ are not in good agreement with the observations, but also not in real conflict with them. Bad agreement between observations and simulations is achieved with the models $X_{A}3$ and $X_{D}3$. In the former model, the resulting $\lambda6825$ line flux is too weak and the spectropolarimetric line structures disagree with the 'typical' observations. Model $X_{D}3$ produces Raman lines with too much flux and not enough line polarization.

It can be concluded from the Rayleigh and Raman scattering simulations that a model with an ionization geometry between B3 and C3 would be most appropriate. The Rayleigh eclipse observations would suggest an 'average' geometry closer to B3, while the Raman line observations are more in agreement with geometry C3. This may be a selection effect, as the Rayleigh scattering eclipse observations are biased towards low-mass-loss systems with short but pronounced minima, while the Raman line observations favour systems with extended scattering regions. An 'average' geometry between model B3 and C3 corresponds to an X-parameter in the range $X_{H^+} = 0.4$–4. For $X_{H^+} = 0.8$, the ionization front looks like a plane which is perpendicular to the binary axis. We recall that this 'average' geometry should be considered cautiously, because it is only a two-dimensional (rotationally symmetric) approximation to a three-dimensional problem.

The given range for the X-parameter is rather restrictive when considering photoionization models. It is recalled that the X-parameter is linked via the employed photoionization model to the binary separation p, ionizing photon luminosity of the hot component L_{H^+}, and the wind parameters of the cool giant $\dot{M}$ and v_∞ (Section 3.1.1). Considering the heterogeneity of the symbiotic class, it is surprising that the combination of these systems parameters $X_{H^+} \sim pL_{H}$ $(v_\infty/\dot{M})^2$ should give for most symbiotic systems a value of around 1. This may suggest that some sort of feedback mechanism is active in symbiotic systems, which supports such an equilibrium ionization geometry.

Alternatively, we may also suspect that other processes are important for producing such an 'average' shape of the interface between neutral and ionized regions. For example, in the interacting wind model of Girard & Willson (1987) the shape of the shock front can be described by the momentum flux ratio $mw = \dot{M}_h v_h / \dot{M}_c v_c$ between the stellar winds from the hot component (index h) and the cool giant (index c). Assuming that the shock front coincides with the interface between neutral and ionized regions, then the 'average' geometry ($X_{H^+} \approx 0.4$–4) corresponds to a momentum ratio in the range $mw \approx 0.1$–10. This seems to be a reasonable range to accommodate a large variety of symbiotic systems.

5.4 Comparison with the *X*-parameter determination of Mürset et al.

Mürset et al. (1991) derived X_{H^+}-parameters for a representative sample of symbiotic systems. They determined the ratio Q^H between the number of recombinations in the emission nebula and the number of ionizing photons emitted from the hot component. The result is $Q^H = 1$ if all ionizing photons interact with the red giant wind, and $Q^H < 1$ if ionizing photons escape from the system. The derived Q^H-values are then converted to an X_{H^+}-parameter, using the same ionization model as in this paper.

Mürset et al. obtained in 11 out of 18 cases a value $X_{H^+} \le 1/3$, while $X_{H^+} \approx 1$–4 for six systems and $X_{H^+} \approx 7$–10 in the remaining object. The result that a large fraction of symbiotic systems have a geometry with $X_{H^+} \le 1/3$ is not supported by the present simulation of the Raman line polarization. Such X_{H^+}-values imply a geometry where the neutral region completely surrounds the hot component, as in model $X_{D}3$. In particular, the $X_{H^+} \le 1/3$ determinations for the systems HBV 475 and AG Dra by Mürset et al. are, according to this paper, not compatible with the large polarization of 3.9 per cent for AG Dra and 4.9 per cent for HBV 475 and the corresponding spectropolarimetric structure, as measured by Schmid & Schild (1994). The simulations on Rayleigh scattering in Paper II also showed that the continuum radiation from the hot star in model $S_{D}3$ would show a strong attenuation near the Lyα transition during the entire orbital phase. This is certainly not observed in the bright systems RW Hya and AG Dra, for which Mürset et al. determined $X_{H^+} \le 1/3$.

It seems to be premature to search for an explanation for the discrepancies described above before more experience with the interpretation of Rayleigh and Raman scattering observations has been gained. However, it should be noted that Mürset et al. obtain $X_{H^+} \approx 1$–4 for the three D-type systems in their sample. The results for the D-type systems are in general agreement with the findings of this paper. Thus the discrepancies between this paper and the analysis in Mürset et al. may be restricted to S-type systems.

6 CONCLUSIONS

This paper presents Monte Carlo simulations for the Raman-scattered emission lines for a wide range of model parameters. The simulations calculate the Raman and Rayleigh scatterings of O VI photons from the emission nebula in the extended neutral wind of the red giant. The adopted scattering geometries are based on the ionization equilibrium formulation of Seaquist et al. (1984) and Nussbaumer and Vogel (1987). Although this description of symbiotic systems is certainly simplified, it can account for most basic properties of the observed Raman lines $\lambda\lambda6825$ and 7082. This includes line strengths, flux variations, polarimetric line structure and phase-locked polarization changes.

The simulations demonstrate that the Raman-scattered lines are most useful for determining the geometric structure in symbiotic systems. The polarization signal provides direct information on the position of the irradiated scattering region relative to the light source. This diagnostic potential is significantly enhanced by the simultaneous presence of measurable Doppler shifts introduced by the systematic motion of the scatterers. A further advantage is that the binary system rotates, so that we get views of the scattering region from different directions.

The present paper compliments a previous similar study on the Rayleigh scattering effects in symbiotic stars (Paper II). Together they form a comprehensive computational

assessment of H^0-scattering effects in symbiotic systems. The model results from both studies suggest that the 'average' symbiotic system has an ionization structure between model geometry B3 and c3, i.e., an X-parameter around $X_{H^+} \approx 1$. Roughly speaking, this 'average' shape of the ionization front does not differ strongly from a plane between the two stellar components. The shape of the ionization front may not only be caused by photoionization alone, but also by other interaction phenomena.

Discrepancies between model results and observations point to some shortcomings of the employed models: two-dimensional instead of three-dimensional models, over-simplified O VI line emission and unsolved uncertainties for the absorption process, especially absorptions by dust particles. All these problems can be investigated with further Monte Carlo simulations. This technique is extremely well suited to investigating the photon-scattering processes in the ionized and neutral regions of symbiotic systems. The formalism is also ideal for the investigation of the three-dimensional scattering geometry. We may therefore expect a major advance in our knowledge on interaction processes in symbiotic systems from future investigations of the Raman-scattered O VI lines.

ACKNOWLEDGMENTS

REFERENCES

Allen D. A., 1979, in Bateson F. M. et al., eds, Proc. IAU Colloq. 46, Changing Trends in Variable Star Research, University of Waikato, Hamilton, NZ, p. 125
Allen D. A., 1980, MNRAS, 190, 87
Allen D. A., 1984, Proc. Astron. Soc. Aust., 5, 369
Cashwell E. D., Everett D. J., 1959, A Practical Manual on the Monte Carlo Method for Random Walk Problems. Pergamon Press, London
Corradi R. L. M., Schwarz H. E., 1993, A&A, 268, 714
Espey B. R., Schulte-Ladbeck R. E., Kriss G. A., Hamann F. W., Schmid H. M., Johnson J. J., 1995, ApJ, 454, L61
Eyres S. P. S., Kenny H. T., Cohen R. J., Lloyd H. M., Dougherty S. M., Davis R. J., Bode M. F., 1995, MNRAS, 274, 317
Girard T., Willson L. A., 1987, A&A, 183, 247
Haniff C. A., Scholz M., Tuthill P. G., 1995, MNRAS, 276, 640
Harries T. J., Howarth I. D., 1996a, A&A, 310, 235
Harries T. J., Howarth I. D., 1996b, A&A, in press
Isliker H., Nussbaumer H., Vogel M., 1989, A&A, 219, 271
Jordan S., Mürset U., Werner K., 1994, A&A, 283, 475
Kenyon S. J., 1986, The Symbiotic Stars. Cambridge Univ. Press, Cambridge
Mikolajewska J., Friedjung M., Kenyon S. J., Viotti R., eds, 1988, Proc. IAU Colloq. No. 103, The Symbiotic Phenomenon. Kluwer, Dordrecht
Mikolajewska J., Kenyon S. J., Mikolajewska M., Garcia M. R., Polidan R. S., 1995, AJ, 109, 1289
Mürset U., Nussbaumer H., Schmid H. M., Vogel M., 1991, A&A, 248, 458
Mürset U., Jordan S., Walder R., 1995, A&A, 297, L87
Nussbaumer H., Vogel M., 1987, A&A, 182, 51
Nussbaumer H., Vogel M., 1990, A&A, 236, 117
Nussbaumer H., Walder R., 1993, A&A, 278, 209
Paresce F., Hack W., 1994, A&A, 287, 154
Sadeghpour H. R., Dalgarno A., 1992, J. Phys. B, 25, 4801
Schild H., Schmid H. M., 1996, A&A, 310, 211
Schmid H. M., 1989, A&A, 211, L31
Schmid H. M., 1992, A&A, 254, 224 (Paper I)
Schmid H. M., 1995, MNRAS, 275, 227 (Paper II)
Schmid H. M., Schild H., 1990, A&A, 236, L13
Schmid H. M., Schild H., 1994, A&A, 281, 145
Schmutz W., Schild H., Mürset U., Schmid H. M., 1994, A&A, 288, 819
Schmidt-Kaler Th., 1982, in Landolt-Börnstein, New Series, Group IV, Vol. 2b, Spirnger, pp. 1 and 449
Seaquist E. R., Taylor A. R., Button S., 1984, ApJ, 284, 202; erratum: ApJ, 317, 555
Vogel M., 1991, A&A, 249, 173
Walder R., 1993, PhD thesis, ETH Zürich No. 10302
Webster B. L., Allen D. A., 1975, MNRAS, 171, 171
Whitelock P. A., 1987, PASP, 99, 573